NONLINEAR PHOTOEMISSION IMAGING

Michael D. Jones
A.B., Washington University, St. Louis, 1972
A.M., Washington University, St. Louis, 1974

A dissertation submitted to the faculty
of the Oregon Graduate Center
in partial fulfillment of the
requirements for the degree
Doctor of Philosophy
in
Applied Physics

November 21, 1980

The dissertation "Nonlinear Photoemission Imaging" by Michael D. Jones has been examined and approved by the following Examination Committee:

GAIL A. MASSEY, Thesis Advisor
Professor

J. FRED HOLMES
Professor

DOUGLAS F. BAROFSKY
Associate Professor

LYNWOOD W. SWANSON
Professor

ACKNOWLEDGEMENTS

I would like to express my gratitude to Dr. Gail Massey for his support and encouragement during my years at the Oregon Graduate Center. I also thank Joel Johnson for his skillful assistance in both technical and nontechnical matters.

Thanks are also due to Nancy Christie for typing this dissertation. Finally, I wish to thank Dr. Eugene Feenberg and Lissa Rippey for their understanding and encouragement.

TABLE OF CONTENTS

LIST OF TABLES

LIST OF ILLUSTRATIONS

ABSTRACT

NONLINEAR PHOTOEMISSION IMAGING

Michael D. Jones, Ph.D.
Oregon Graduate Center, 1981

Supervising Professor: Gail A. Massey

Nonlinear photoemission mechanisms have been investigated for GaAs and $LiNbO_3$ and their nonlinear photoelectric yield characteristics have been obtained. These yields were achieved using several different sample preparation techniques. GaAs was used as a bare, polished crystal with or without a thin layer of cesium applied to the surface. The $LiNbO_3$ samples investigated were polished crystals coated with a thin tungsten layer alone, or with an additional thin layer of cesium. The coatings used were measured to have thicknesses very much less than visible light wavelengths; guided waves propagating in $LiNbO_3$ or GaAs substrate were able to penetrate the coating layer. The current densities required for high resolution imaging can be produced by the nonlinear emission in these materials with optical intensities below the damage threshold. Simple, low-resolution electron optics have been used to form images of waves propagating in samples of GaAs and $LiNbO_3$.

An ultraviolet illuminator suitable for linear photoemission microscopy has been developed and used to obtain high resolution electron micrographs at wavelengths of 266 and 213 nm. This ultraviolet source is useful for obtaining an image of the sample to be studied using nonlinear emission and also provides illumination for operator adjustment of the electron optics.

The aberrations introduced into photoelectron emission imaging by the use of high current density electron beams have been considered. A variety of physical processes occuring in the anode-cathode space in the photoelectron microscope have been analyzed and the parametric dependence of the image aberrations has been found. These results indicate that aberrations will introduce image blur of less than ~ 500 Å for current densities as high as 1 A/cm^2 in narrow beams. Nonlinear photocurrent densities much less than 1 A/cm^2 are needed for submicron imaging, and these space charge dependent aberrations should not be limiting factors in obtaining image resolutions down to 500 Å.

CHAPTER 1

INTRODUCTION

The research presented in this dissertation is concerned with the development of the techniques and theory required to image localized optical fields at the surfaces of materials by using nonlinear photoemission as a probe. Nonlinear photoemission yields have been measured for GaAs and $LiNbO_3$, and electron optical images of light beams propagating in these materials have been obtained. An ultraviolet illuminator suitable for focusing a high resolution photoelectron microscope in which the nonlinear emission is to be observed has been made. In addition, the aberrations introduced into electron optical imaging systems by the use of the pulsed electron beams produced by the pulsed laser required to generate the necessary nonlinear photoemission have been calculated.

The idea of using photoelectrons to produce an image of an emitting surface is not new; the first photoelectron microscope was demonstrated in 1933.[1] Since then vacuum techniques and the resolution attainable with electron optics have improved tremendously, so that instruments operating in the pressure range 10^{-9} - 10^{-10} torr with resolution down to 120 Å have been demonstrated.[2,3] This type of microscope is particularly useful because its transverse resolution is much better than that of an optical instrument and its depth resolution (~ 50 Å) is better than that of conventional scanning or transmission electron microscopes. Of course it also displays different information in its images, which are actually maps of quantum yield and light intensity distributions. Photoelectron microscopes have been used primarily in the field of metallurgy, although recently they have been used to image integrated circuits[4] and biological samples.[5] The work presented here represents an extension of photoelectron microscopy to the imaging of photoelectrons produced by nonlinear mechanisms which permits the exciting light beam or beams to propagate inside of the sample of interest.

There are three applications foreseen for the techniques presented here:

1. The engineering development of integrated optical devices;
2. The understanding of light induced damage to components in high intensity laser systems; and
3. The exploration of small scale vector diffraction effects near the boundaries of conducting objects.

These applications require the viewing of either guided waves near the surface of an integrated optical structure, or evanescent optical fields surrounding defects (or other details) at the surfaces of optical materials of all kinds. It is a characteristic of these fields that they contain spatial variations on a substantially smaller scale than the free-space wavelength of light, and because this optical energy is confined or evanescent, it cannot be imaged by optical instruments at practical distances from the surface. Although it is possible to view visible radiation in some guide materials by means of light scattered from defects in the material, this scattered light is subject to the usual diffraction limit of image resolution and cannot reveal the evanescent phenomena. Conventional electron lenses provide resolutions on the order of tens of angstrons, and the photoemitted electrons can be focused by such lenses to form an image of the localized surface intensity distribution.

Integrated optical devices are to be one of the primary subjects of the imaging techniques described in this dissertation. The field of integrated optics has been a field of intense study since about 1968. With expected improvements in fabrication methods, e.g., using ultraviolet, x-ray, or electron/ion beam lithographic techniques, it should be possible to make structures much smaller than a light wavelength. These features can affect the optical fields in much the same way as lumped-parameter circuits at radio frequencies. The use of nonlinear photoemission as a probe permits the mapping of guided photon densities in the presence of such small perturbations. Two materials commonly used in integrated optical devices are GaAs and $LiNbO_3$ and these are the materials whose nonlinear emission characteristics were studied. Intense optical beams in these materials have been shown to produce nonlinear photoemission.

The second application mentioned above is the study of damage to optical components by intense laser beams. It is believed that small defects in an optical surface can be accompanied by localized fields greater than the average incident field, with the result that breakdown occurs at these points first. Using reasoning similar to that employed by Crisp[6] in explaining the enhanced damage susceptibility of the exit faces of materials, Bloembergen[7] has also considered the local field enhancement near surface defects such as microscopic cracks, pits, and bubbles. By applying the well-known electrostatic depolarizing factors to these shapes he has shown that large reduction in the damage threshold will result. Minute absorbing impurities, difficult to observe with ordinary optical instruments, may also play a role in optical damage phenomena. Photoelectric imaging of such defects can provide a useful nondestructive diagnostic tool in optical damage investigations. Note that the type of damage which can be studied by this means is not bulk damage but surface damage caused by avalanche or multiphoton ionization at sites of physical defects in the surface.

The third potential application of the work is to an area of more fundamental optical science. Photoelectric imaging provides an experimental means of exploring small-scale vector diffraction effects near the boundaries of conducting objects at optical frequencies. The standard assumptions of scalar diffraction theory are violated in this domain and this method can provide experimental data on which more accurate calculations can be compared.

In the next chapter, nonlinear photoemission studies of GaAs and $LiNbO_3$ are presented. Chapter 3 is concerned with the requisites for the use of the nonlinear emission in a high resolution photoelectron microscope. Chapter 4 discusses ultraviolet illuminators for use in focusing such an electron microscope and contains the results of imaging experiments carried out on GaAs and $LiNbO_3$ with optical beams propagating in the samples. The concluding chapter summarizes the results obtained and suggests the direction in which further research efforts should be made.

CHAPTER 2

NONLINEAR PHOTOEMISSION

In this chapter the experimental results obtained for nonlinear photoemission yields on GaAs and $LiNbO_3$ will be presented. First, the experimental context for this work will be given, so that the measurements obtained in this work may be compared with the nonlinear photoemission studies of previous workers. Second, the currently accepted theoretical models of the photoemission process will be discussed. Third, the general approach taken in the experiments done for this dissertation will be outlined, including descriptions of the special problems associated with nonlinear photoemission. The experimental apparatus used will be described in detail. Finally, nonlinear photoemission yield results for the two materials of interest will be presented.

2.1. Experimental Background

The first experimental observation of nonlinear photoemission was reported by Sonnenberg, Heffner, and Spicer[8] in 1964. They found a two-photon photoelectric effect in Cs_3Sb, which was the photocathode in a commercial (1P28) phototube. The photoemission was produced by the radiation of a Nd:glass ($h\nu = 1.17$ eV) laser. This experiment was followed by reports of nonlinear photoemission in other materials. Workers observed nonlinear photoemission in the alkali antimonides

Cs_3Sb and K_3Sb,[9] in CsI,[10] and in a variety of metals.[11-14] The results of several of these experiments are summarized in Table 2-1. Where the data permitted, the relationship between laser intensity and photoelectric current density has been included. This is of the form $J = \beta I^n$, where J is the photoelectric current density, β is a constant of proportionality which includes such things as electron escape depth and nonlinear absorption coefficient, and n indicates the number of input quanta required to produce the electron emission. Relationships of this same form for GaAs and $LiNbO_3$ will be discussed later.

The results of earlier workers presented in Table 2-1 provide a basis for the work presented here, but there are several important differences which make the problems associated with the nonlinear photoemission (and the subsequent imaging of the emission) in GaAs and $LiNbO_3$ more difficult. In order to understand these problems it is useful to summarize briefly those properties which are expected of high yield photoemitters:[15,16]

1. High optical absorption coefficient;
2. Large escape depth for the photoexcited internal electrons; and
3. Low surface barrier, i.e., small or negative electron affinity E_A.

A large escape depth is anticipated for materials in which the electrons are able to move to the surface without the loss of energy. For materials with the band gap $E_G < E_A$, those electrons which have

TABLE 2-1

NONLINEAR PHOTOEMISSION YIELDS FOR VARIOUS MATERIALS

Material	Photon Energy (eV)	Yield Equation (J in A/cm^2, I in W/cm^2)
Cs_3Sb	1.17	$J = 7.6 \times 10^{-12} I^2$
CsI	1.7 + 6.5 to 8.0	---
K_3Sb	1.78	$J = 3.0 \times 10^{-13} I^2$
Ta	2.33	$J = 1.0 \times 10^{-17} I^2$
Au	1.78	$J = 1.0 \times 10^{-25} I^2$
Au	3.56	$J = 2.4 \times 10^{-15} I^2$
Na	1.48	$J = 1.3 \times 10^{-19} I^2$

been excited into the conduction band and have energy $E_G + E_A$ are sufficiently energetic to raise additional electrons to the conduction band via electron-electron collisions. Thus, the excited electron falls to the bottom of the conduction band where it is no longer able to be emitted. Generally, materials with $E_G/E_A > 1$ are expected to be good photoemitters (and secondary emitters). The other main mechanism which limits the electron escape depth is electron-phonon scattering. Individual electron-phonon scattering events cause only small reductions in electron energy.

In contrast to the work displayed in Table 2-1, the studies done here with GaAs and $LiNbO_3$ use exciting light beams at wavelengths for which the materials of interest are nominally transparent. This is, in fact, essential to the application that has motivated this research, but it is in contradiction to the first requirement for high yield emission stated above. For example, radiation of photon energy 1.17 eV has been used for this study on GaAs, which is essentially transparent to photons of this energy. We must rely on the multiphoton absorption coefficient to provide the necessary supply of hot electrons to be emitted. A second feature apparent in the data of Table 2-1 which contrasts with this work is that several of the materials used in these earlier studies are high yield electron emitters, i.e., they are used commercially as photocathodes (Cs_3Sb) or are known to be high yield materials (CsI). Both Cs_3Sb and CsI have E_G/E_A ratios of less than one, and we therefore expect that the electron escape depth is large. One of our materials (GaAs) has a ratio $E_G/E_A = 2.93$ and the other ($LiNbO_3$) has a more favorable ratio. Finally, in our work, we are attempting to image samples (and eventually integrated optical devices) which may not be cleaned in high vacuum by standard techniques without causing the sample to alter its optical or waveguide properties. The materials used in the earlier studies were either formed in high vacuum or capable of being cleaned in high vacuum without being altered in any essential way. For diagnostic experiments in integrated optics it is not convenient to fabricate the devices in the vacuum in which they are to be examined.

2.2. Photoemission Theory

It is instructive to briefly review the basic theory of photoemission in order to estimate yields of an design experiments on GaAs and $LiNbO_3$. Photoemission from metals was treated theoretically, using an approach that evolved from the Sommerfeld free electron model of a metal, in which a continuous band of states is filled to a level E_F, the Fermi energy. In this early work, photoemission was assumed to be a surface effect, i.e., the momentum required to maintain momentum conservation was supplied by the step potential of the surface. It was hoped that this model would predict both the both the photoelectric yield as a function of photon energy and the energy distribution of the photoelectrons. Eventually it was recognized that the photoelectric effect was also a volume effect and could be used to determine the nature of the periodic potential in which the electrons of a solid move. Kane[17] showed that the band structure of crystalline materials could be found from measurements of the energy and momentum distributions of the photoelectrons, and this idea ultimately resulted in ultraviolet photoelectron spectroscopy and x-ray photoelectron spectroscopy techniques. The main theoretical basis used in this dissertation was provided by a model in which the photoemission process is assumed to result from three distinct steps:[18]

1. Absorption of a photon and creation of an excited electron;
2. Transport of the electron to the surface; and
3. Transmission of the electron through the surface barrier.

More recent theoretical approaches[19] treat both surface and volume photoemission simultaneously by using a wave-mechanical scattering theory. The three-step model, however, will be used as an approximate model for the purposes of the present work.

The materials used in this work, GaAs and $LiNbO_3$, have band structures and photoemission properties typical of semiconductors and insulators, respectively. Although the energy bands in GaAs have been extensively studied,[20,21] little is known about the detailed band structure of $LiNbO_3$.[22] The single-photon photoelectric threshold for clean GaAs is about 5.5 eV,[23] and for $LiNbO_3$ it is between 3.9 eV and 4.6 eV, depending on orientation because of the polarization in that material.[24] GaAs has a band gap of 1.4 eV, so that wavelengths below 900 nm are strongly absorbed, whereas significant absorption in $LiNbO_3$ does not begin until the photon energy exceeds about 3.7 eV. Because of these differences in absorption edge and electron affinity, freely propagating photons in GaAs can have only about 25% of the energy needed for photoemission, yet photons can propagate in $LiNbO_3$ with up to 90% of the threshold energy. This suggests that different multiphoton excitation mechanisms must be exploited in working with the two materials, as indicated in Figures 2-1 and 2-2.

The lower energy bands and the escape energy (vacuum level) for electrons moving in the [110] direction in GaAs are indicated in Figure 2-1, along with two possible nonlinear photoemission processes. Process (a) is multiphoton excitation of a valence electron to a conduction band above the vacuum level. It is in general nonresonant, except for energy conservation between initial and final electron states, and the photon energy must be less than the band gap energy. Process (b) uses two photons at different frequencies. The energetic photons are used to populate a band just below the vacuum level, from which the other photons, which have less than the gap energy, can excite electrons to a band above the vacuum level. In the context of the imaging application here, the low-energy photons are propagating in the GaAs, and the high-energy photons are incident on the surface as a uniform pump illumination from outside the crystal. The advantage of process (b) is that the photoemission is linearly related to the propagating beam intensity. This process has been used previously in the study of alkali halide crystals.[25,26]

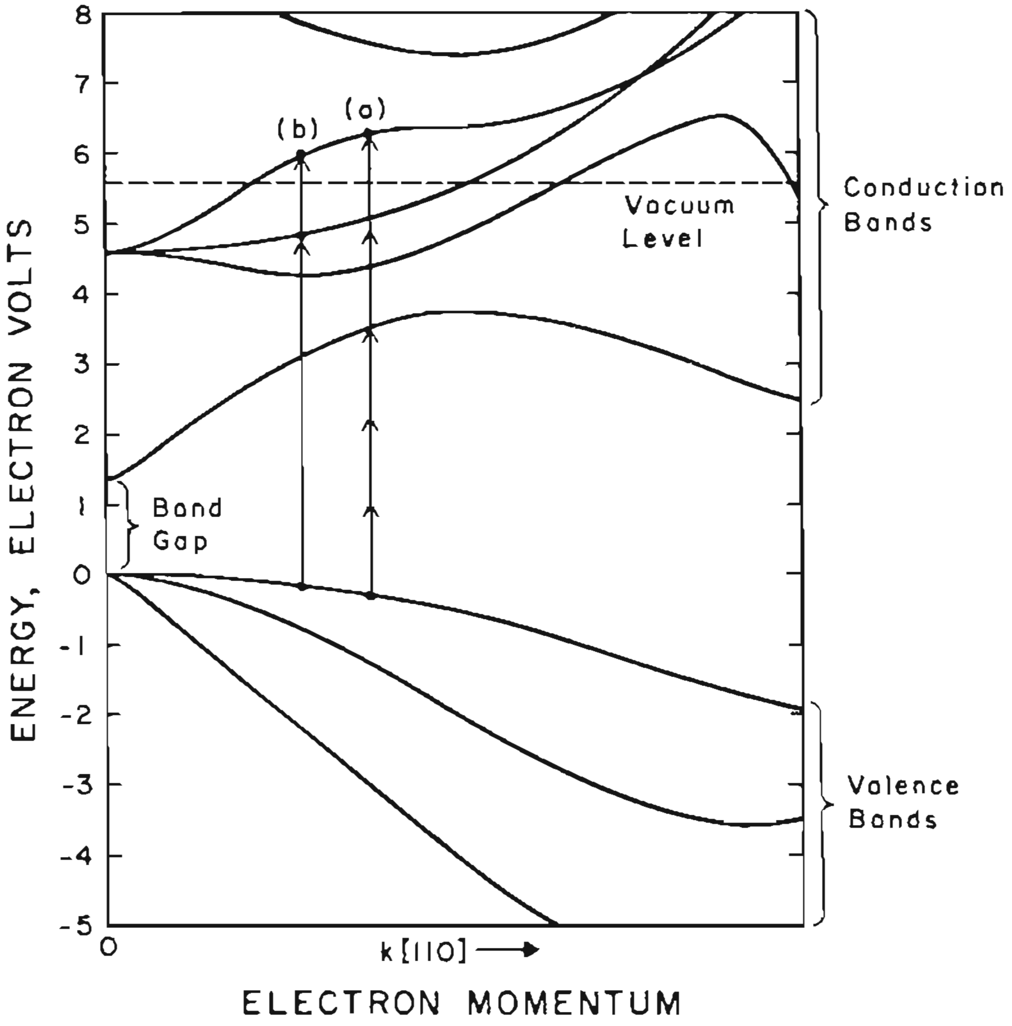

Figure 2-1. Band structure and photoemission mechanisms for (110) oriented GaAs. Five-photon, single-frequency absorption is indicated by (a) two-photon ultraviolet assisted absorption is shown as (b).

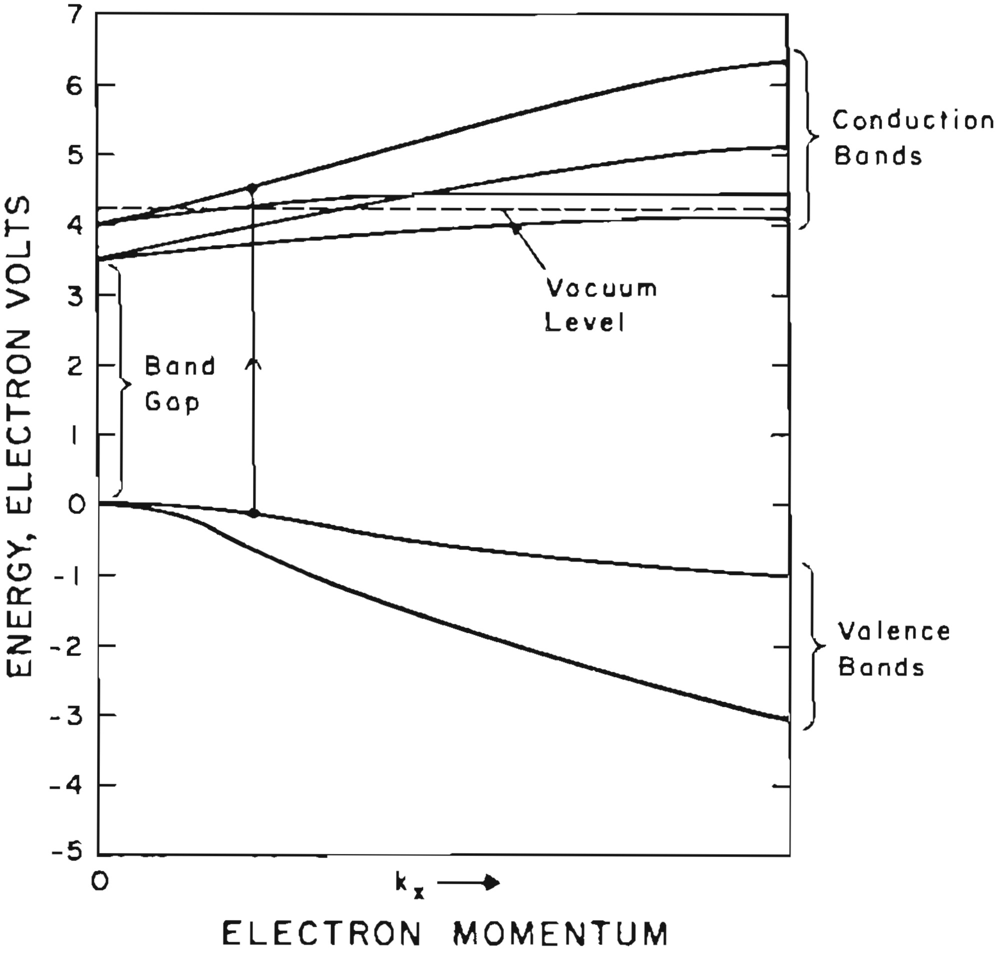

Figure 2-2. Hypothetical bands and emission mechanism for x-directed electrons in $LiNbO_3$. The large band gap permits two-photon absorption of propagating waves.

Figure 2-2 shows hypothetical bands for $LiNbO_3$, since the detailed structure is not yet known. The large band gap permits us to employ low order (two or three photon) nonresonant absorption at a single wavelength. There is little reason to use the resonant two-frequency approach (b) of Figure 2-1 with $LiNbO_3$.

The photocurrent density leaving the surface due to transitions from a valence band i to a conduction band j can be expressed as

$$J_{ij} = T_j(\bar{k}) \int dz \, \exp(-\alpha z) \left[\int \frac{2}{(2\pi)^3} \, d^3k \, W_{ij}(\bar{k}, z) \right] \tag{2-1}$$

where $W_{ij}(\bar{k},z)$ is the per-electron induced transition rate at $\bar{k}$ in the Brillouin zone and at depth z below the surface, α is the reciprocal of the mean free path for electrons in band j at $\bar{k}$, and $T_j(\bar{k})$ is the escape transmission coefficient at the surface. Experiments with various coatings of known thickness having photoelectric thresholds in the 4-6 eV range show that the mean free path of electrons with these energies is of the order of 50 Å. Photoelectron microscopy is based on the excellent depth resolution implied by this parameter. The surface transmission coefficient approaches unity for electrons reaching the surface near normal incidence if their energy is more than a few tenths of an eV above the vacuum level.

When a single frequency is incident, the W corresponding to a nonresonant m-photon interaction in a multilevel system is:[27]

$$W_{ij}^{(m)} = \frac{\pi \, g_{ij}(m\omega) \, |S|^2}{2^{2m-1} \, \hbar^{2m}} \tag{2-2}$$

where

$$S = \sum_{\substack{q,p,\ldots b,a \\ \text{all bands}}} \frac{H'_{jq}\, H'_{qp} \ldots H'_{ba}\, H'_{ai}}{\left[(m-1)\omega-\omega_{qi}\right]\left[(m-2)\omega-\omega_{pi}\right]\ldots\left(2\omega-\omega_{bi}\right)\left(\omega-\omega_{ai}\right)} \qquad (2\text{-}3)$$

$$H'_{xy} = \sqrt{\frac{L}{3}}\, \mu_{xy}\, E(z)\, e^{i\omega t} \qquad (2\text{-}4)$$

and $$g_{ij}(m\omega) = \frac{1/\left(\pi\tau_{ij}\right)}{\left(m\omega-\omega_{ij}\right)^2 + \left(1/\tau_{ij}\right)^2} \; . \qquad (2\text{-}5)$$

Above L is the local field correction factor, τ_{ij} is the effective lifetime of a dipole between i and j, μ is the electric dipole moment between j and i at $\bar{k}$, and E is the optical field at frequency ω that exists at a depth z. This corresponds to process (a) in Figure 2-1.

If two frequencies ω_{iq} and ω_{qj} are used to excite an electron resonantly from $|i\rangle$ to $|q\rangle$ and finally to $|j\rangle$, the transition rate can be written in the more compact form

$$W_{ij}^{(2)}(\bar{k},z) = \frac{\sigma_{iq}\,\sigma_{qj}\,\tau_q\, I_{iq}\, I_{qj}}{\hbar^2\, \omega_{iq}\, \omega_{qj}} \qquad (2\text{-}6)$$

where the I's are the optical intensities at ω_{iq} and ω_{qj}, τ_q is the lifetime of the intermediate state $|q\rangle$, and the σ's are cross sections[28] of the form

$$\sigma_{xy} = \frac{\omega_{xy}\, \pi\, L\, |\mu_{xy}|^2}{3\, n\, \epsilon_o\, c\, \hbar} \cdot \frac{1/(\pi\tau)}{\left(\omega-\omega_{xy}\right)^2 + (1/\tau)^2} \qquad (2\text{-}7)$$

where n is the crystalline refractive index, ϵ_o is the permittivity of space, and the other symbols have their usual meanings. This corresponds to process (b) in Figure 2-1.

Of course it is difficult to use these theoretical results quantitatively, because that would require knowledge not only of all the band energies for all $\overline{k}$, but, in addition, the dipole matrix elements between the bands for every point in k space. However, they do serve as a guide to designing experiments and interpreting results.

In the case of $LiNbO_3$ one can use the empirically measured two-photon absorption coefficient to estimate the photocurrent resulting from that process. The light-induced absorption coefficient is βI cm^{-1}, where I is the light intensity in MW/cm^2 and β is the two-photon coefficient in cm/MW. The published value[29] for β is about 2×10^{-3} cm/MW for $LiNbO_3$ in the visible. If we take γ to be the efficiency of generating photoelectrons from absorbed photons, and L to be the electron mean free path near the threshold energy, the photocurrent density can be written

$$J = \gamma \beta I^2 L \; e/\hbar\omega \; . \qquad (2\text{-}8)$$

2.3. Experimental Nonlinear Photoemission

Nonlinear photoemission yield studies have been carried out on GaAs and $LiNbO_3$ to determine the intensities and wavelengths that must be employed to obtain photocurrents large enough for imaging applications. The general approach of these investigations was to find a relationship of the form $J = \beta I^n$ (where J, β, I, n are the same as defined earlier) for processes of the type (a) in Figure 2-1, or $J = \beta I_1^{n_1} I_2^{n_2}$ for processes of type (b) in Figure 2-1, where the subscripts refer to the different wavelengths. An optical pulse (or pulses) of known total energy was allowed to strike a sample and the total emitted charge was measured. In no case was a time resolved measurement of the emission current made. Measurements of this type would require bandwidths much greater than 10 MHz and the resulting increase in noise level due to both Johnson noise and background pickup would cause an unacceptable lowering of detector capability.

Several constraints were taken into consideration in performing the experiments. First, the input optical beam was to produce intensities of .1 to 10 MW/cm^2, necessitating the use of a pulsed laser. Second, the optical intensity was to be kept below the damage threshold of the material used. The intensity required to cause damage is a function of optical pulse length and wavelength, and for the pulse lengths used in this work (10-200 ns), the intensity must be kept below about 100 MW/cm^2. (The largest possible spot sizes and confocal distances were used in these experiments so that the intensity at the sample could be accurately determined.) Also, even if the average pulse intensity is below the damage threshold, the pulse may cause damage if it contains fluctuations in intensity which are appreciably greater than 100 MW/cm^2. Third, the intensity must be kept low enough to prevent sample heating and thermionic emission. This is especially important for work done with metal coated speciments as the metal coating can strongly absorb radiation at wavelengths at which the underlying GaAs or $LiNbO_3$ is transparent. Even with nearly transparent metal coatings, the metal coating will tend to heat more readily than the substrate. In addition, for samples treated with a cesium layer the work function may be lowered to below 2 eV, which would allow sizeable thermionic emission currents even at rather modest temperatures. For example, a reduction in work function from 4 eV to 2 eV at a temperature of 1000 K causes the thermionic current density to rise from $\sim 10^{-16}$ A/cm^2 to $\sim 10^{-6}$ A/cm^2. For the laser spot sizes and pulse lengths used in this work a current density of 10^{-6} A/cm^2 would correspond to $\sim 10^{-15}$ Coulomb of thermionically emitted charge, a value comparable to the expected amount of photoemission. The maximum temperature rise produced on a metal coated $LiNbO_3$ sample surface at the center of the laser beam by 532 nm radiation can be found from the relation[30]

$$\Delta T(r,t) = I(1 - R)(k\rho c)^{-1/2}\ \tau^{1/2}\ 2^{-1/4}\ \eta(t/\tau)\ \exp[-(r/d)^2] \quad (2\text{-}9)$$

where I is the maximum laser intensity, R is the reflectivity, k is the thermal conductivity, ρ is density, c is heat acpacity, d is the laser beam diameter, τ is the laser pulse length, t is the time, and $\eta(t/\tau)$ is a function evaluated in the reference cited. For the case of interest here $k = .0046$ W/cm/°C, $\rho = 19.3$ g/cm^3, $c = .13$ J/g/°C, and $\eta \approx 1.5$. Substituting these values into equation (2-9) and assuming 1% absorption in the metal layer and $\tau = 100$ ns gives $\Delta T/I = 1.68 \times 10^{-5}$. To obtain a temperature rise to 1000 K we then must have $I = 42$ MW/cm^2. This is higher than the intensities used in the experiments; thus we expect negligible thermionic emission.

Finally, it was necessary to eliminate electrical signals which did not originate from photoemission but which are synchronous with the optical pulses. These artifacts include the pyroelectric and piezoelectric effects. The pyroelectric coefficient of $LiNbO_3$ is approximately 4×10^{-9} Coulomb/cm^2/°C so that a temperature rise of 10^{-3} °C in an area equal to a typical beam area of 10^{-2} cm^2 would give an apparent emitted change of 4×10^{-14} Coulomb. Electrical signals produced by these effects were identified by reverse biasing the sample so that true electron emission was suppressed and any residual signal was attributable to a non-emission effect. It was also possible to verify that certain signals were not produced by electron emission by allowing the pressure in the vacuum chamber to rise to a point where the mean free path of the electron is very small compared to the distance it must travel to be collected.

Yet one more feature of the experimental yield work was the non-linearity of the sought-after processes. Given that the relationship between beam intensity and current density was to be established by measurements of pulse energy and total emitted charge, it was necessary to use beams with reproducible spatial and temporal envelopes. For a pulse of fixed energy, E, beam area A and variable pulse length τ, an n-photon process will produce an amount of emitted charge proportional to $(E/A\tau)^n A\tau = E^n/(A\tau)^{n-1}$ and a variation $\Delta\tau$ in pulse length changes the collected charge by a factor $(n-1)\Delta\tau/\tau$ which is zero only for linear emission. If τ is not constant, or, if the temporal envelope of the pulse is not constant, pulses with the same pulse energy can produce different quantities of charge. This implies that measurements of pulse energy are not adequate to determine pulse power. This was a serious problem with one of the lasers used in this work, as will be discussed later. A similar argument is true in regards to beam area but the spatial profile of the beam is easily controlled with apertures in the cavity of the laser oscillator.

Study of highly nonlinear emission also requires a large signal-to-noise ratio and dynamic range in the detection apparatus. For a high order process with $n = 4$, an attenuation of the input pulse energy by a factor of two results in a reduction in collected charge by a factor of $2^{-4} = .063$. For lower-order processes this problem was not so acute.

2.3.a. Light Sources

As mentioned above, the light sources used in producing nonlinear photoemission must be capable of producing very intense reproducible optical beams. If large spot sizes are to be used, the laser must be pulsed to obtain sufficient intensity. Nd:YAG lasers and a variety of nonlinear crystals for generating various harmonics were chosen for this research. The fundamental 1064 nm radiation ($h\nu =$ 1.17 eV) of this laser was ideally suited for studies of GaAs, which has a band gap cutoff wavelength near 900 nm. The photoelectric work function of GaAs is 5.5 eV so that 4.3 eV are required to produce photoemission in conjunction with 1064 nm radiation. The

Nd:YAG fourth harmonic at 266 nm ($h\nu = 4.68$ eV) appeared to be ideally suited for this application. The photoelectric threshold of $LiNbO_3$ is also easily reached with the fourth harmonic of this laser.

Two different Nd:YAG laser systems were used in this work. One was a flash pumped, Q-switched oscillator-amplifier system, and the other was a continuously pumped, repetitively Q-switched laser. The flash pumped laser consisted of a 6 mm diameter 75 mm long laser rod pumped by a xenon flashlamp whose flash duration was 100 μsec. The rod was in a resonator 75 cm in length, terminated by flat mirrors, one of which served as the output coupler and transmitted 50% of the incident 1064 nm radiation. The resonator also contained a 1.4 mm diameter aperture and a dielectric polarizer. The laser was Q-switched by a deuterated KDP electro-optic crystal in which a longitudinal electric field was used. The laser typically generated an average power of 20 mW at a repetition rate of 10 Hz. The pulse length was 10 ns and the peak power produced was about 300 kW. Single pass amplification of this beam in another flash pumped Nd:YAG rod was employed in some of the experiments. The shot-to-shot variation in pulse energy was usually about 10%, but the variation in pulse power was much greater.

Preliminary nonlinear photoemission studies carried out with the flash pumped Nd:YAG laser indicated the presence of a very high order, strongly intensity dependent photoemission process. Since it was expected[31] that the pulses from this laser might contain subnanosecond power fluctuations, a study of the temporal structure of the pulses was made. The pulse envelope was expected to show the usual intermode harmonic frequencies produced by interferences among the various longitudinal modes of the resonator. The high gain produced in the Nd:YAG crystal by flash pumping broadens the laser gain profile and enhances the likelihood of temporal fine structure in the pulse envelope on subnanosecond time scales. If the temporal envelope varies significantly from pulse to pulse, laser peak power cannot be reliably inferred from measurements of pulse energy.

The picosecond structure of the flash pumped Nd:YAG laser output was studied with a Hamamatsu streak camera system (Model 145 Temporalanalyzer and C979 Temporal Disperser) with resolution of 10 psec. This device operates by allowing the optical signal to be examined to strike a photocathode and then sweeping the photoelectrons across a detector system. The photocathode of the streak tube used here was an S-20 type without infrared response at 1064 nm; thus the Nd:YAG fundamental was frequency doubled to 532 nm to match the photocathode sensitivity. The longest pulse which could be viewed with this streak camera is 10 ns so the middle of the laser pulse was selected and the leading and trailing edges were not detected. Many optical pulses were examined and two representative examples are shown in Figure 2-3. The 532 nm pulse usually displayed only the lowest order mode beats when viewed with a fast photodiode and oscilloscope with 500 MHz bandwidth. Even within this bandwidth, the temporal profile is not constant. However, the streak camera data clearly show that

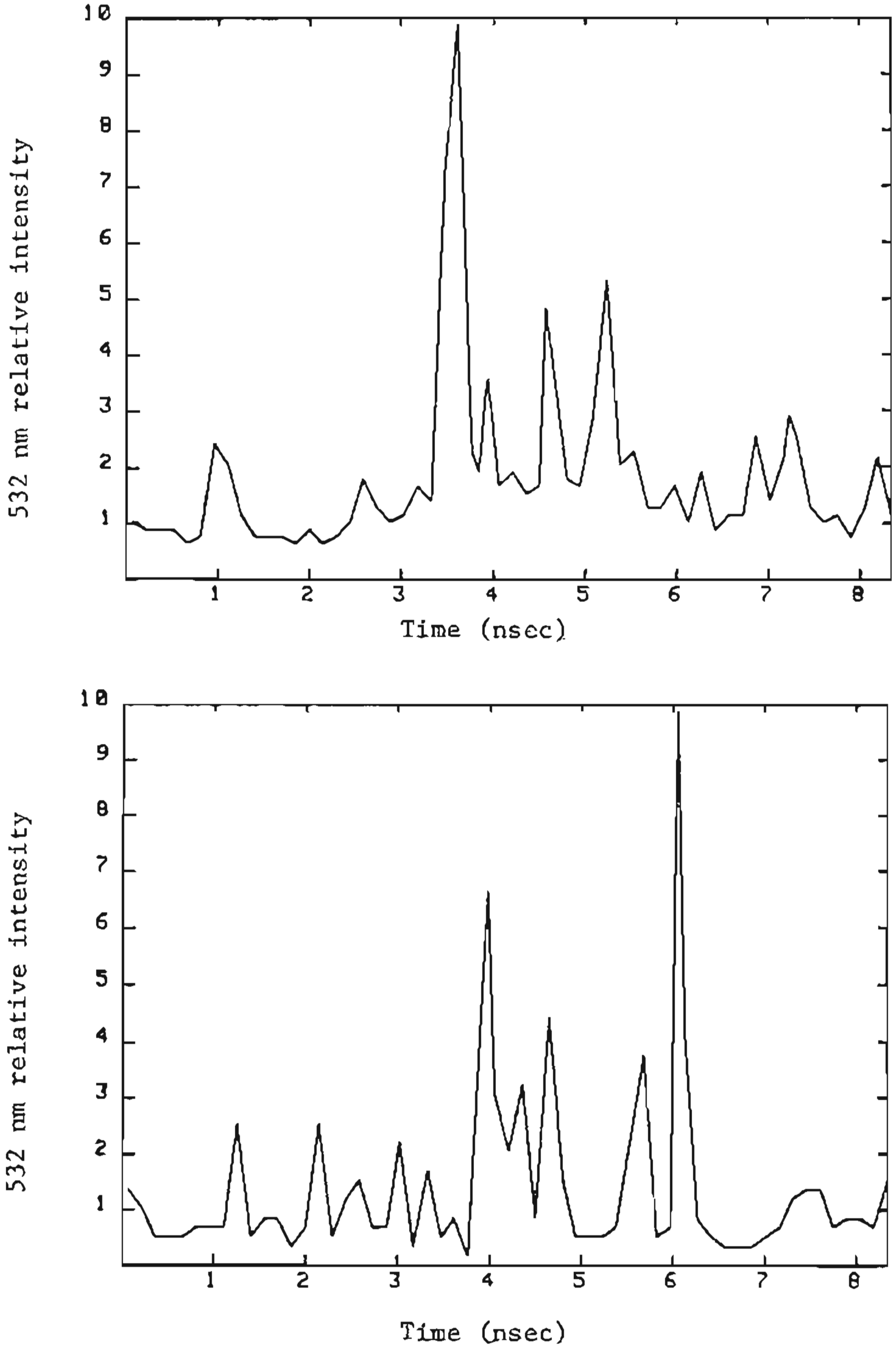

Figure 2-3. Pulse shapes produced by the flash-pumped Nd:YAG laser.

the pulses of this laser often contain much of their energy in spikes of short (≈ 200 psec) duration. The laser power during these spikes is 5 to 10 times higher than its pulse-average peak power. Pulses of this type are of doubtful utility in quantifying any nonlinear effect when only the total energy (or photoelectric charge) can be detected by the measuring apparatus.

In order to determine the extent to which this laser could be used reliably in the work presented here, functions of the form $\int_{\text{pulse}} I^n dt$ were evaluated numerically for several laser pulses and different values of n. The streak camera data for each pulse were first normalized so that $\int_{\text{pulse}} I' dt = 1$, where I' is the normalized intensity. Then, the integral $\int I'^n dt$ was evaluated on a computer for $n = 2$ and $n = 4$. For comparison, the same calculations were done on a square pulse. The results are shown in Table 2-2. Since the data used were based on the pulses at $\lambda = 532$ nm, the power laws for processes involving the fundamental $\lambda = 1064$ nm would be 2, 4, 8 respectively. The table shows that although the pulse shapes are highly irregular, they seem to be reasonably consistent in that $\int I'^4 dt$ does not fluctuate appreciably for the different pulses. (A similar calculation involving a slightly different flash pumped Nd:YAG laser was done; again, the pulses were irregular but the $\int I'^n dt$ values were reasonably self-consistent, though different from the values for the laser used in this work.) For processes involving powers of I_{1064} greater $n = 4$ however, the data are likely to appear random when these lasers are used.

TABLE 2-2

VALUES OF $\int I^n dt$ FOR FLASH-PUMPED LASER PULSES

Pulse No.	$\int I^2_{532} dt$	$\int I^2_{532} dt$	$\int I^4_{532} dt$
1	1.00	.018	$.22 \times 10^{-4}$
2	1.00	.018	$.39 \times 10^{-4}$
3	1.00	.016	$.17 \times 10^{-4}$
Reference	1.00	.083	$.58 \times 10^{-6}$

The other laser employed in this work was a continuously pumped, repetitively Q-switched Nd:YAG laser. It typically produced 300 mW of 1064 nm average power at a repetition rate of 1.5 kHz. The pulse length was 100 ns and the peak power was 2 kW. This laser can also produce the same average power at the second harmonic 532 nm by the insertion of a $LiIO_3$ crystal inside the laser cavity and changing the output coupling mirror to transmit 532 nm and reflect 1064 nm. The overall pulse envelope was essentially Gaussian but did contain mode beats. Because of the longer pulses and lower gain of this laser, subnanosecond fluctuations are much less pronounced than in the flash pumped laser. The shot-to-shot energy variation was less than 5%. This laser was used in experiments to make an ultraviolet illuminator for conventional photoelectron microscopy and will be described in more detail in Chapter 4.

The flash-pumped Nd:YAG laser was best suited to experiments in which only the photoelectron charge of a single pulse was detected, while the cw-pumped laser was capable of producing higher average currents. Assuming that both lasers are focused to produce the same intensity and, therefore, the same current density, the cw-pumped laser must be focused to an area 150 times smaller, based on the peak powers available from each laser. Since the emitted charge $Q = JA\tau$ the ratio of the charge produced by the flash-pumped laser to that of the cw-pumped laser is $Q_{fp}/Q_{cw} = A_{fp}\tau_{fp}/A_{cw}\tau_{cw} = 15$. The average currents differ by a factor of 15×10 Hz/1.5 kHz = 0.1.

2.3.b. Optical Attenuators, Modulators, and Detectors

Several different techniques were used to vary the optical energy which impinged on the target. In general, modulation of the optical power by changes in Nd:YAG rod pumping level is not appropriate due to the possible variation introduced in both spatial and temporal beam profile as well as a shift in beam position. The continuously pumped Nd:YAG laser rod, in particular, acts as a strong focusing element due to the substantial temperature gradients in the laser crystal. Therefore, the laser used was allowed to operate at fixed settings and was attenuated externally. (The flash-pumped Nd:YAG laser actually required no modulation; its shot-to-shot energy variation produced an adequate range of pulse energies.)

The simplest method of attenuation used was the insertion of a series of metal screens in the beam before it reached the sample. The holes in these screens were much smaller than the beam size but much larger than the wavelength of the light, so that they obstructed part of the beam without appreciably affecting the location of the focused spot. The screens could be cascaded and the insertion of each screen caused a reduction in beam intensity by a factor of about 3 when only the central diffraction order of the transmitted light was used. The screens were calibrated by measuring their attenuation at λ = 632.8 nm. These screens were of somewhat limited utility in the nonlinear work here as the use of even 2 screens in an experiment with two-photon photoemission would reduce the collected charge by nearly a factor of 10. If the original signal to noise ratio were

window which served as the polarization analyzer. This arrangement was capable of producing a modulation of 80% with a 60 Hz envelope imposed on the cw Nd:YAG 1.5 kHz pulse rate. The modulator arrangement is shown in Figure 2-4 and typical modulated cw Nd:YAG laser output is shown in Figure 2-5. This device greatly simplified data only 5-10, the s/n ratio would then be reduced to an unacceptable level.

Another simple method of attenuation is the insertion of a flat glass window or microscope slide in the beam so that the front and back surfaces of the window reduce the power of the transmitted beam. The reflection loss at an air-glass interface ($n_{glass} = 1.5$) is 4% so the total loss is 8%. While this loss was not adequate to investigate low order non-linear processes, it was useful for high order non-linearities. For $J = \beta I^n$, $\Delta J/J = n\Delta I/I$ so for $n = 4$ and $\Delta I/I = .08$ this implies that $\Delta J/J = .32$, which should be easily detectable.

A third type of attenuator used in this work was an electro-optic $LiNbO_3$ crystal. The polarized beam from the Nd:YAG laser was incident on a 5 mm × 5 mm × 2.5 cm $LiNbO_3$ axis, which was along the 2.5 cm dimension of this crystal. A variable, alternating high voltage provided by a neon sign transformer and a Variac was applied to electrodes on the sides of the crystal to produce a field along the x crystallographic axis. The high voltage was adjusted in order to produce a half wave retardation at the maximum voltage of the 60 Hz high voltage. The crystal was followed by a Brewster angle window which served as the polarization analyzer. This arrangement was capable of producing a modulation of 80% with a 60 Hz envelope imposed on the cw Nd:YAG 1.5 kHz pulse rate. The modulator arrangement is shown in Figure 2-4 and typical modulated cw Nd:YAG laser output is shown in Figure 2-5. This device greatly simplified data

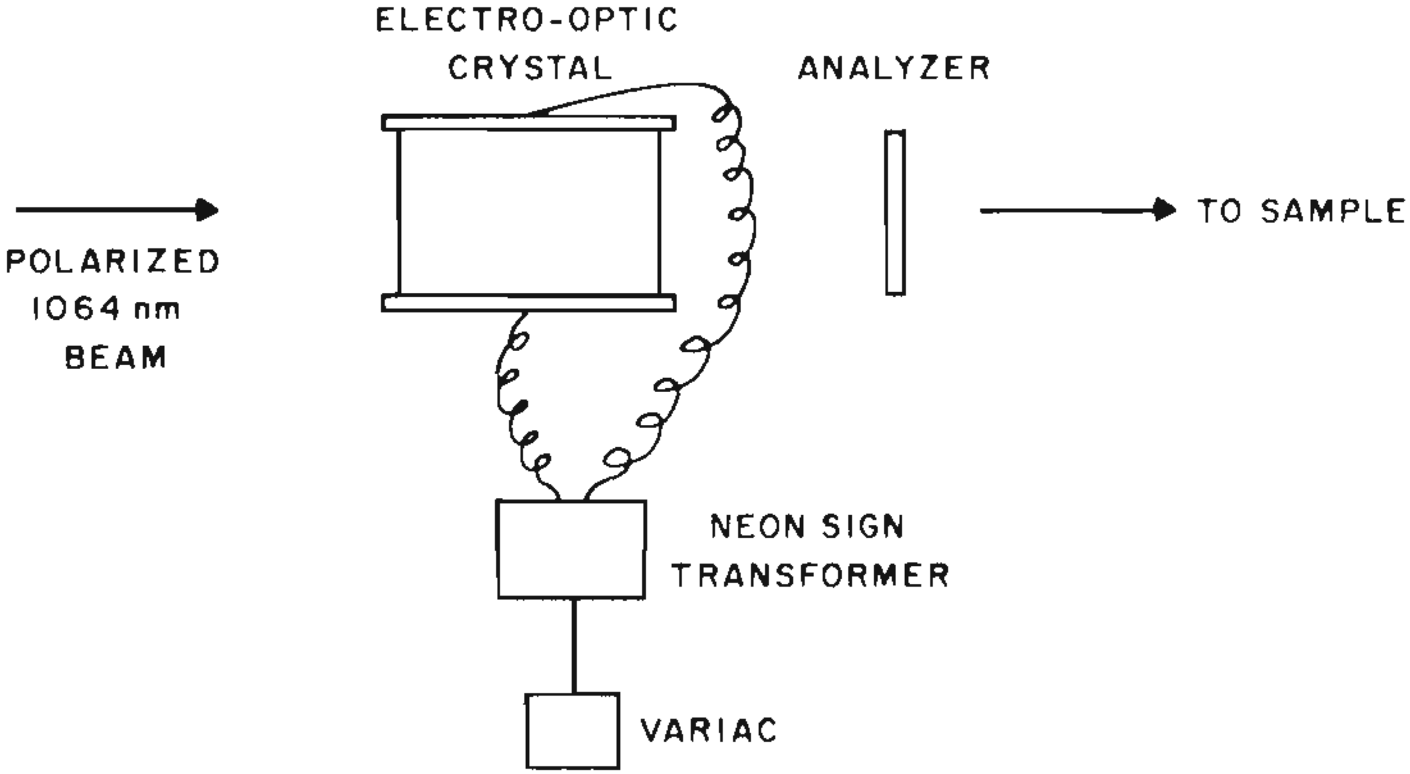

Figure 2-4. Electro-optic modulator for 1064 nm radiation.

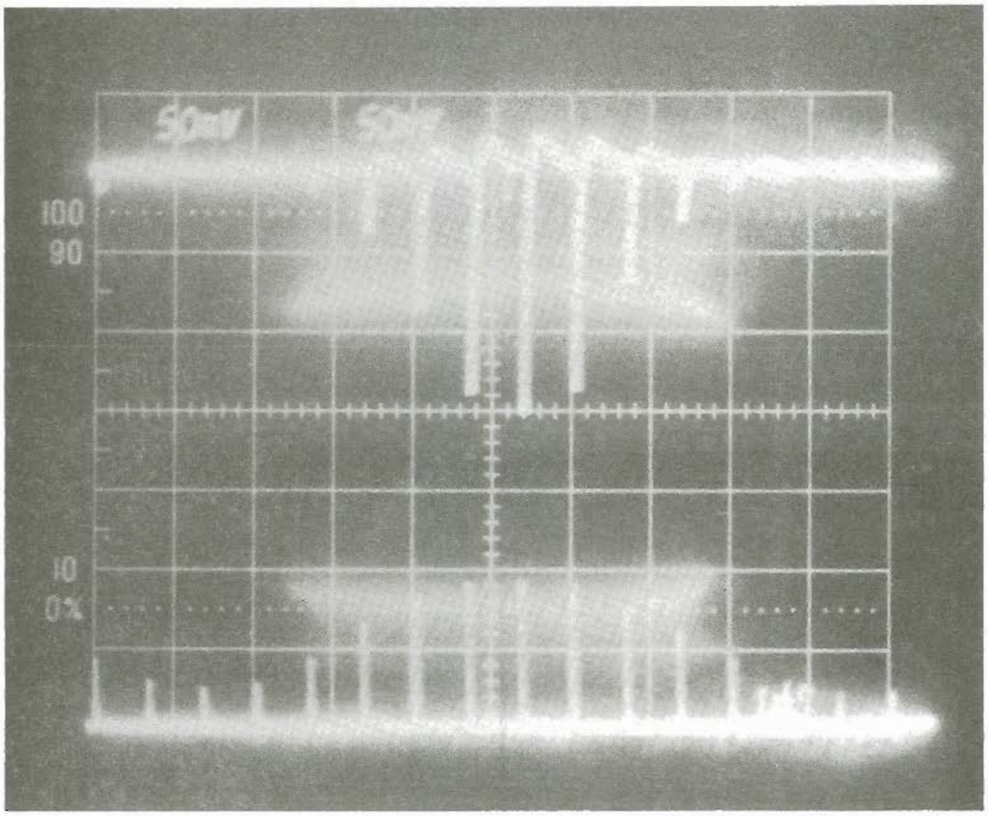

Figure 2-5. Data sample obtained with electro-optic modulator.

collection since pulse energy was varied rapidly and automatically. Using a dual channel oscilloscope and camer at was possible to determine from a single photograph the incident optical energy and corresponding photoemitted charge for several different values of pulse energy. In addition, when the coatings applied to the samples were observed to degrade rapidly, the 60 Hz modulator made it possible to characterize the process very quickly before surface contamination affected the photoemission signal.

2.3.c. Photocurrent Detection

The photoemitted charge was measured either on a pulse by pulse basis or as an average current, depending on the amount of emission. In either case, the total integrated pulse charge was detected with a simple transimpedance amplifier whose circuit is shown in Figure 2-6. The output of this amplifier (for input pulses of duration very much less than the RC time of the feedback loop) is a voltage pulse of amplitude $V_{out} = Q/C'$ where Q = input charge and C' is the feedback loop capacitance. C' was measured by determining amplifier response to known charge inputs and by observing the RC decay time, and was found to be 1.1 pF. On an average basis $\overline{V}_{out} = \overline{I}R = fQR$, when the average current $\overline{I} = fQ$ and f is the pulse frequency. The output of this amplifier was viewed with a Tektronix Model 7904 oscilloscope equipped with a Model 7A22 differential amplifier plug-in. The bandwidth of the amplifier was adjustable between 1 kHz and 30 kHz. The ultimate pulse charge detection limit with this system

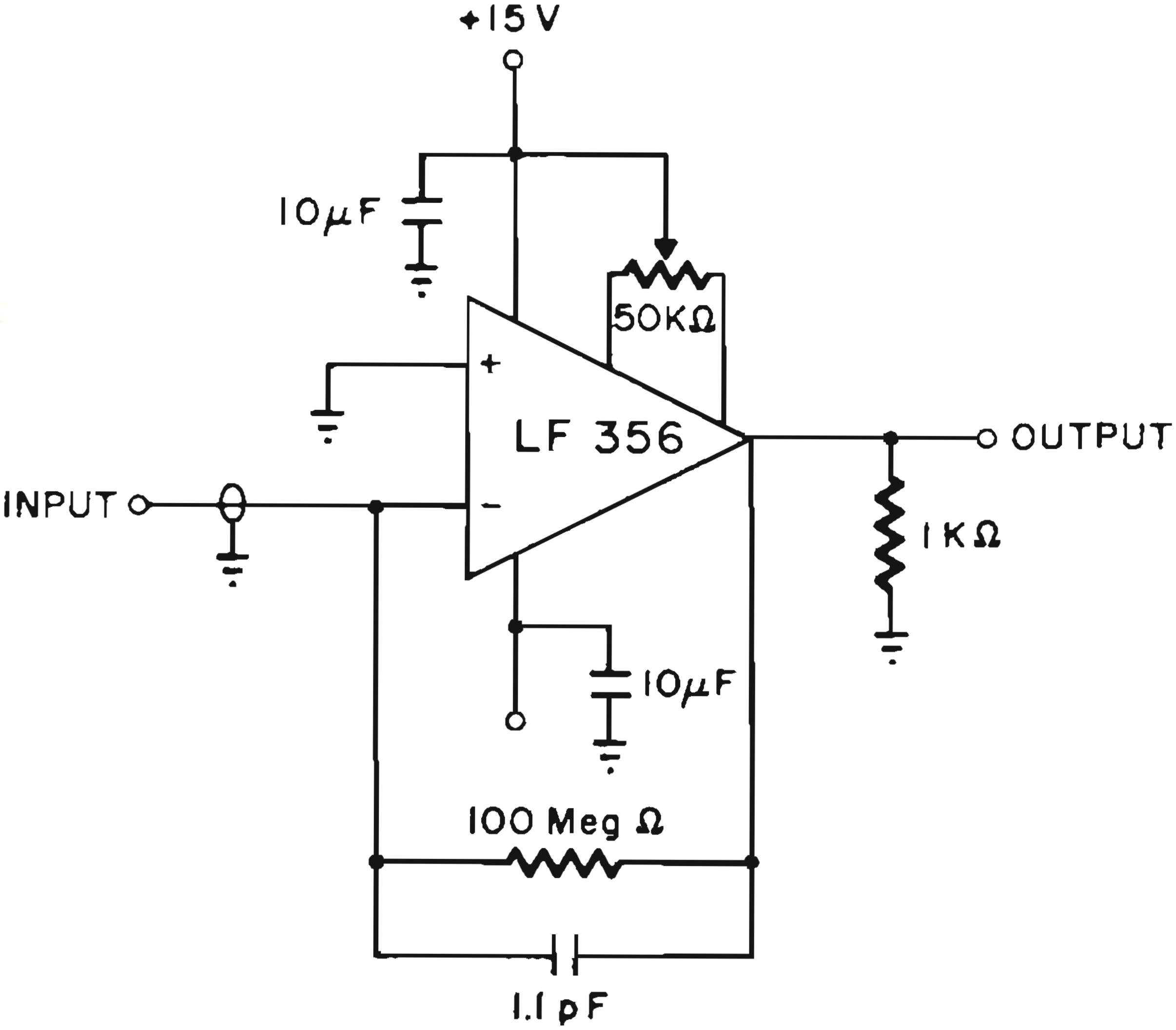

Figure 2-6. Charge sensitive amplifier.

was set by pickup of radio frequency energy produced by the laser Q-switch, and it generally corresponded to a signal level of 5 mV or $Q = 5 \times 10^{-15}$ C. The detection limit could be lowered slightly by using the transimpedance amplifier in conjunction with a Princeton Applied Research Model 5101 Lock-In Amplifier tuned to the laser Q-switch frequency. Using integration times of a few seconds the minimum pulse charge detectable was 2×10^{-15} C with that apparatus.

2.3.d. Optical Intensity Measurements

Optical powers were measured using both slow and fast detectors. Absolute beam average powers (and therefore absolute pulse energies) were measured with Coherent Radiation CR-210 or CR-201 power meters. Relative pulse energies were obtained by using an hpa 4203 fast silicon PIN photodiode and integrating circuitry to yield pulse energy rather than pulse power. This fast detector was calibrated against one of the Coherent Radiation power meters. Typically the photodiode was inserted in a stray beam beyond the optical attenuators so that pulse energy could be monitored without interfering with the main beam. The fast detector was also used to determine the optical pulse lengths and observe the pulse shape (with 500 MHz bandwidth) by viewing the photodiode output with the Tektronix 7904 oscilloscope and a 7A19 amplifier.

Spot sizes were measured at the sample location using a micrometer-driven knife edge and a power meter to determine the 85% and 15% attenuation points. Since the sample position ordinarily was inaccessible in the vacuum chamber, He-He laser beams were arranged to intersect at the sample location so that the chamber could be moved out of the way for these measurements. Apertures were used in the laser resonators to ensure that the transverse mode structure of the beams was TEM_{00}. In addition, the largest possible confocal parameters for the focused beams were used so that longitudinal positioning errors during spot size measurements would not drastically alter the estimated beam sizes.

2.3.e. Sample Description

Experiments with GaAs and $LiNbO_3$ samples were carried out to measure the nonlinear electron emission under various conditions of laser illumination. The GaAs samples were Cr doped (110) oriented crystals with resistivity about 3×10^8 ohm-cm. The $LiNbO_3$ crystals were oriented with the Y and Z crystallographic axes in the plane of the emitting surface. Dimensions of the samples were about 1 cm × 1 cm × 0.05 cm. The faces were optically polished, and tapered facets were also polished on some of the edges so that laser beams could be brought into the slab from the side, making multiple internal reflections against the emission face. The samples were cleaned by a simple procedure using only organic solvents, and were placed in a Varian Model 932-1200 vacuum system capable of reaching 5×10^{-9} torr pressures at the gauge location in the chamber. We believe our samples were subject to higher pressures, probably in the 5×10^{-8} to 5×10^{-7} torr range. Since the application of interest is inspection of fabricated devices, we avoided working with cleaved surfaces and pressures low enough to sustain atomically clean surface for extended periods; such procedures would be necessary, for example, in energy band studies. A fused silica window in the vacuum chamber provided access to the sample for beams of various wavelengths. The sample was mounted in a copper holder about 2 cm from a positively biased anode electrode which served as the electron collector.

2.4. Experimental Results

The current density versis intensity for the (110) face of GaAs illuminated by the 1.064 μm radiation from the flash pumped Nd:YAG laser is shown in Figure 2-7. As expected from the high photoelectric threshold, the yield shows approximately a five-photon characteristic. The data were collected by displaying both pulse energy and pulse charge simultaneously on the y and x axes of an oscilloscope. This recording method compensates for the shot-to-shot variation in energy but does not eliminate inaccuracies due to the changeing temporal envelope of the pulse as discussed earlier. For this very high order process the existing variation in laser energy was sufficient to generate the desired range of data without a variable attenuator. The laser beam was focused by a single lens to a spot of area .02 cm^2. The highest intensities approach the damage threshold for the material; however, the corresponding current

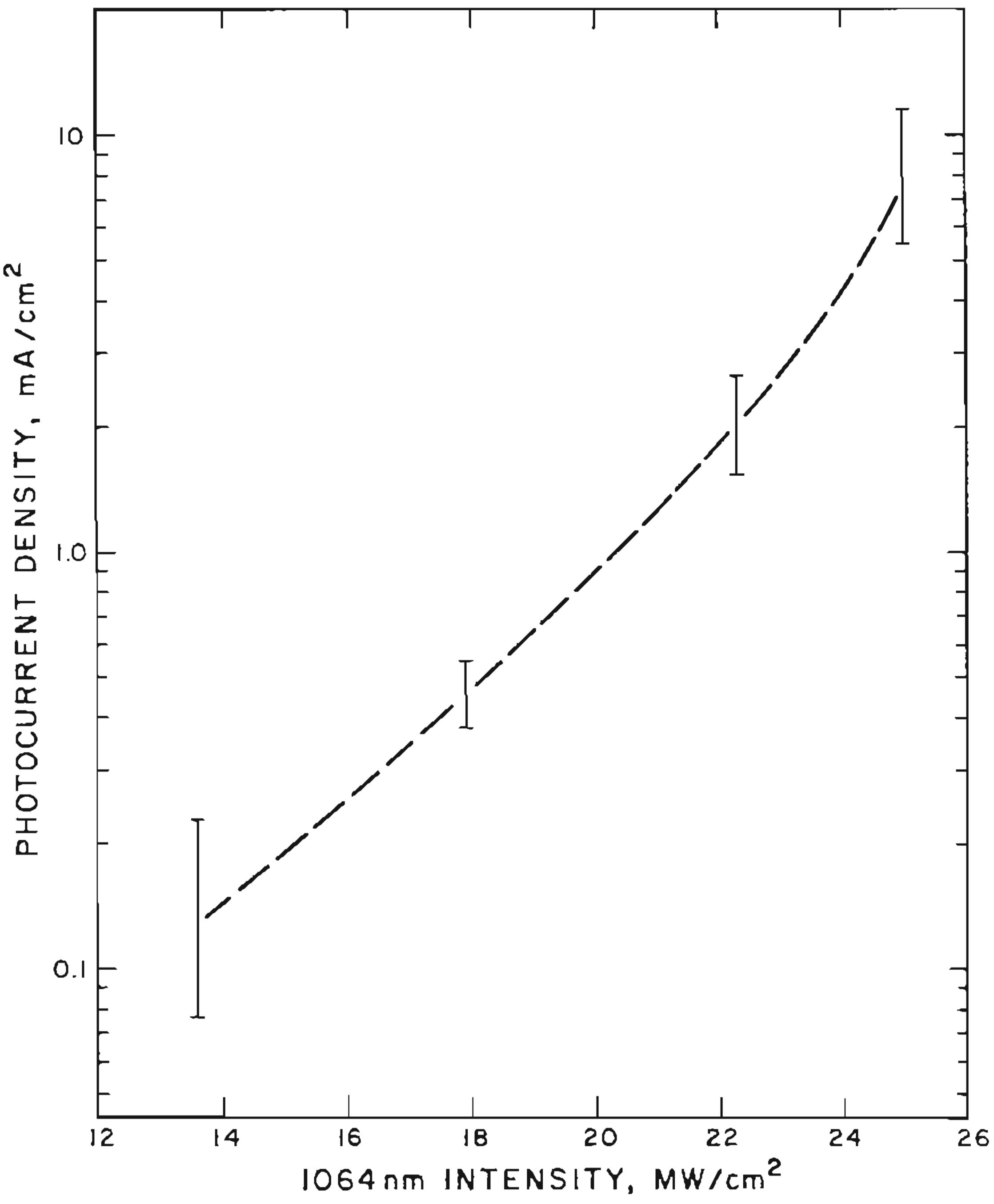

Figure 2-7. Photocurrent density vs. laser intensity at 1064 nm for (110) faces of GaAs.

densities were more than adequate to provide high resolution images according to the theory presented in Chapter 3.

Attempts to observe the two-photon process (b) of Figure 2-1 in GaAs were unsuccessful. We employed coincident beams at 266 nm and at 1064 nm on our sample; the intensity at each wavelength was separately controlled. The expected photocurrent component should have been present only when both wavelengths struck the sample. In fact. we obtained linear emission at a quantum efficiency of about 2×10^{-6} from the 266 nm alone, and no additional current was seen due to 1064 nm until intensities corresponding to multiphoton infrared absorption (Figure 2-4) were reached. Apparently there is not a sufficient density of states with energies close to resonance for this wavelength combination to provide a useful nonlinear photocurrent. Experiments with ultraviolet from a xenon arc lamp together with a 1064 nm laser beam also showed no significant effect due to the type (b) process. Of course the spectral density and intensity of the arc are much less than those of the laser fourth harmonic. It is possible that type (b) emission from GaAs might be observed using the tunable ultraviolet second harmonic of a visible dye laser; we have not attempted that experiment.

In order to reduce the electron affinity of the GaAs sample, a thin layer of cesium was applied. Results for the cesiated GaAs are shown in Figure 2-8. The slope indicates a three-photon effect, and the intnesities required to produce current densities comparable to those of the five photon emission are much lower. The data were

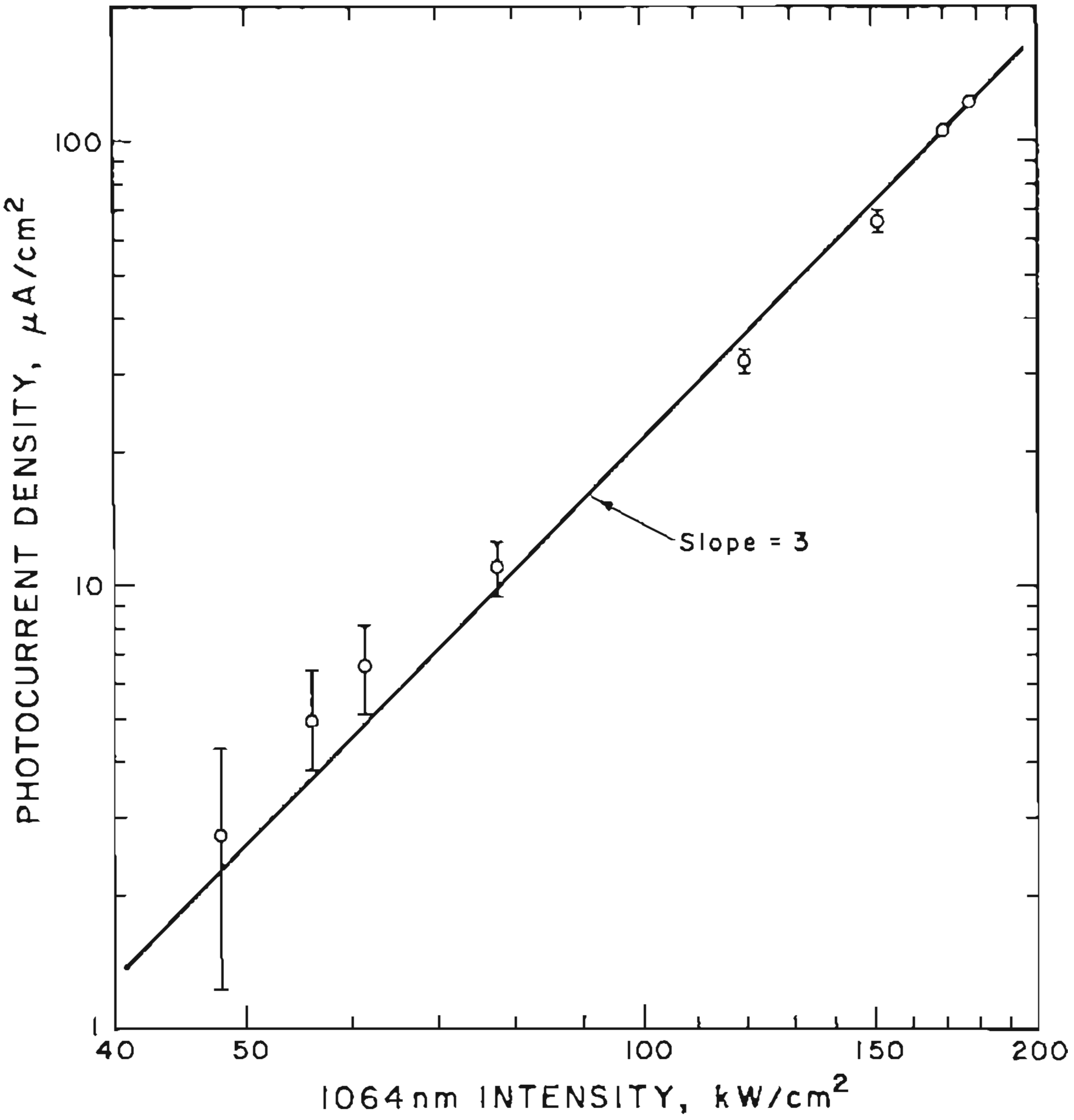

Figure 2-8. Photocurrent density vs. laser intensity at 1064 nm for cesiated (110) GaAs. Slope indicates most emission is by three-photon absorption.

obtained using the continuously pumped laser and the $LiNbO_3$ modulator described earlier. The beam was focused to an area of .02 cm^2. The thin cesium layer was found to produce negligible absorption of light propagating near the surface of the GaAs. The thickness of the layer and the method by which it was applied are discussed in Chapter 3. The lowered photoemission threshold produced by the cesium was observed to degrade in a matter of several minutes, probably due to surface contamination at the pressures used in these experiments. Note that the application of cesium under high vacuum conditions should reduce the threshold to 1.4 eV so that a 2-photon process should be possible.

The nonlinear emission characteristic of $LiNbO_3$ was also investigated, but in order to prevent charge accumulation the samples were coated with a thin layer of a slightly conducting material. Several different thin metallic coatings were tried as discussed in Chapter 3. The nonlinear emission characteristic of tungsten-coated $LiNbO_3$ at $h\nu = 2.34$ eV is shown in Figure 2-9. The data were obtained with the continuously pumped Nd:YAG laser, which was internally frequency doubled with a $LiIO_3$ crystal. The beam was focused to an area of .007 cm^2. The emission was measured with the PAR lock-in amplifier and transimpedance amplifier. Metal screen attenuators were used to vary the optical intensity. The tungsten surface film had a resistance of about 30 kΩ. This layer does not reduce the photoemission threshold energy, but it does result in photocurrent densities corresponding to γ values near one in eq. (2-8), assuming the electron

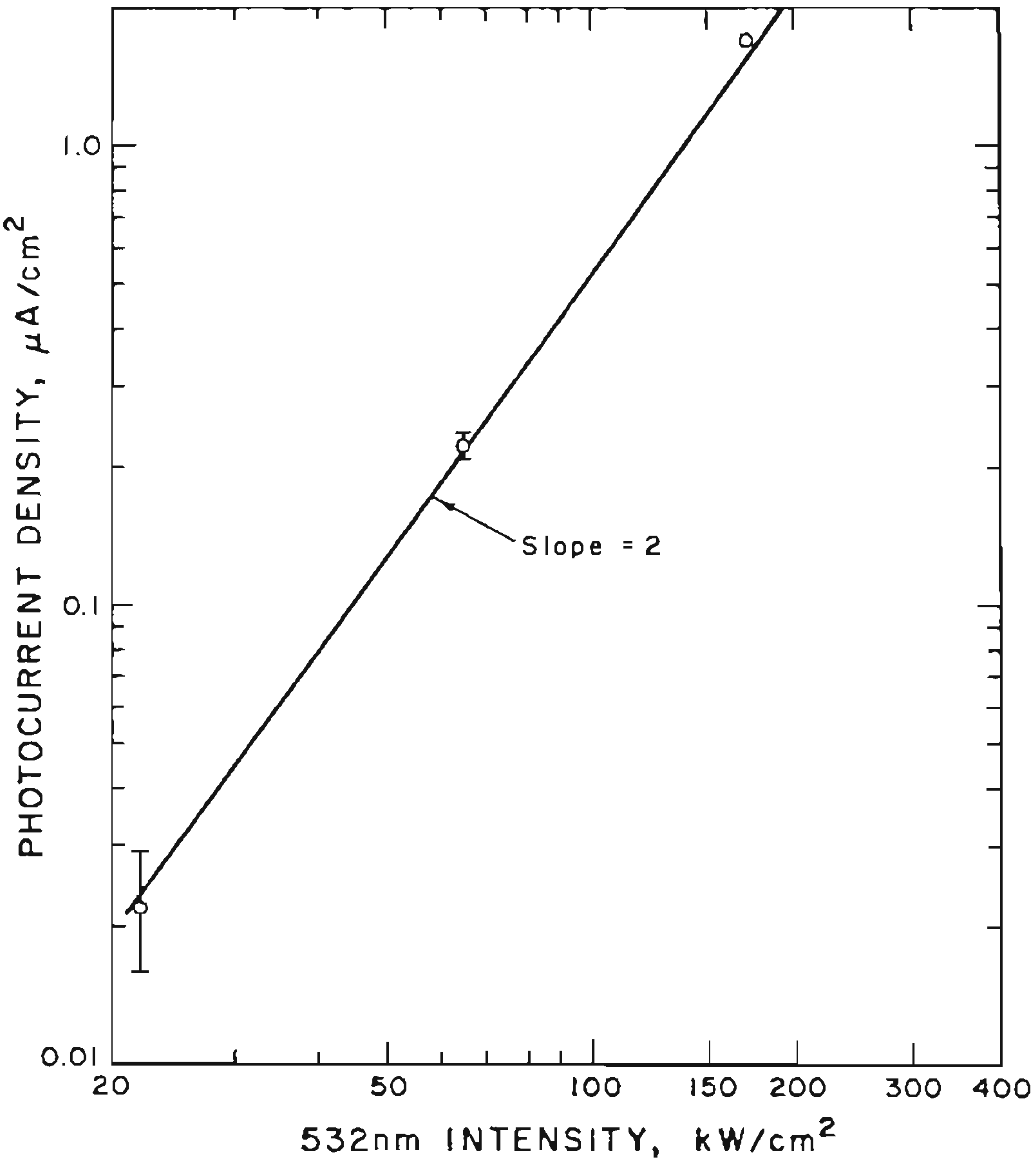

Figure 2-9. Photocurrent density vs. intensity for tungsten-coated $LiNbO_3$. Emission is via two-photon absorption. Experiment for low resolution imaging of guided waves in $LiNbO_3$ or GaAs wafers.

escape depth L is about 50 Å. The emission was stable over periods of many hours under the vacuum conditions of our experiments. This implies that ample time would be available to study such a surface under high electron optical magnification, and that maintaining sufficiently high vacuum in the sample chamber of the microscope should not be a problem.

Addition of a cesium layer to the tungsten coated $LiNbO_3$ produced a surface with a linear photoemission yield in the visible. At 532 nm we found that the yield was 3×10^{-5} electron/incident photon. The total, single-pass absorption of this coating was less than 5%. This result demonstrates the interesting possibility of having simultaneously a substantial linear photoelectric response from a sample which has very low loss for wavelengths propagating within it.

The results of these experiments are summarized in Table 2-3 for comparison with the nonlinear photoemission studies of previous workers. The results for cesiated GaAs show it to be a considerably better photoemitter at 1.17 eV (3 photon process) than gold is at 1.78 eV. Also, we can see that the magnitude of the two-photon emission of $LiNbO_3$ at 532 nm is comparable to the two-photon processes of Table 2-1, if the alkali antimonides are excluded. The results shown in Table 2-3 will be used in conjunction with the imaging theory presented in Chapter 3 to determine the optical intensities and duty factors required for successful, high resolution electron imaging.

TABLE 2-3

NONLINEAR PHOTOEMISSION YIELD SUMMARY FOR GaAs AND $LiNbO_3$

Material	Photon Energy (eV)	Yield Equation
GaAs	1.17	$J \sim 2.6 \times 10^{-40}\ I^5$
GaAs (cesiated)	1.17	$J \sim 2.1 \times 10^{-20}\ I^3$
$LiNbO_3$ (coated)	2.34	$J \sim 5.2 \times 10^{-17}\ I^2$
$LiNbO_3$ (coated and cesiated)	2.34	$J \sim 1.3 \times 10^{-5}\ I$

CHAPTER 3

IMAGING OF PULSED ELECTRON EMISSION

The use of photoelectric emission to form images of sample surfaces was first demonstrated in 1933[32] and had been anticipated even earlier.[33] More recently images of metal surfaces under ultraviolet arc lamp illumination have been obtained with resolution down to 120 Å[34] and biological surfaces have been examined with better than 500 Å[35] resolution. In conventional photoelectron microscopy the illumination is uniform and the sample properties vary spatially; thus the electron image contains information about the sample. Alternatively if the sample is uniform but the optical intensity varies, the the photoelectric image would be a high resolution map of the surface intensity pattern. In the application of interest here, the objective is to image this surface intensity pattern. Ultraviolet illumination is used to produce photoemission as individual photons are energetic enough to produce photoelectrons. The application to guided or evanescent waves requires that light beams be used at wavelengths which are only weakly absorbed by the samples being studied. It is therefore necessary to use very intense optical beams. This suggests the use of pulsed sources; however, the small area of a low-order optical waveguide does permit the attainment of MW/cm^2 intensities with some continuous lasers. A more compelling reason for considering the pulsed source case is that a much greater diversity of wavelengths presently is available with pulsed laser technology, particularly in the ultraviolet.

The purpose of this chapter is to outline the basic requirements for and limitations to the high resolution imaging of the nonlinear photoelectric emission. The fundamental limits imposed on the current densities required for imaging are introduced and problems associated with the use of an insulating sample such as $LiNbO_3$ are discussed. A solution to this problem is described. Finally, the various aberrations which limit the resolution of the photoelectron microscope are analyzed, including those resulting from the use of pulsed electron emission.

3.1. Current Density and Resolution

Because of statistical fluctuations in the amount of charge emitted by each resolution element on the sample during an exposure time, the resolution (d), current density (J), exposure (T), and minimum contrast are related. If we assume Poisson emission statistics, for which the variance in number of photoelectrons is equal to the mean, and if we take the minimum contrast C to be the ratio of the standard deviation of total charge from a resolution element to mean charge emitted by that element, we obtain the minimum current density

$$J_0 = e/\eta d^2 C^2 T. \qquad (3\text{-}1)$$

Above η is the fraction of emitter current from an elemental area d^2 collected by the electron optics. As an example, suppose the maximum practical exposure time is 100 seconds, the resolution is 10^{-5} cm, the minimum contrast is 0.1, and the collection efficiency is 0.1. The corresponding J_0 is 1.6×10^{-8} A/cm^2. This value assumes continuous illumination; if the experiment is pulsed the peak current density must be larger, inversely related to the duty factor.

The duty factors of the two pulsed lasers used in this study are 10 ns × 10 Hz = 10^{-7} and 100 ns × 1.5×10^3 Hz = 1.5×10^{-4} for the flash pumped and the continuously pumped laser respectively. The corresponding J_0's for the duty factors are 1.6×10^{-1} A/cm^2 and 1.1×10^{-4} A/cm^2. Referring to Figures 2-7, 2-8 and 2-10 and selecting the continuously pumped laser as the more suitable illuminator due to its larger duty factor, it is seen that optical intensities of ~ 13 MW/cm^2 for GaAs at 1064 nm (5-photon process), ~ .16 MW/cm^2 for cesiated GaAs at 1064 nm (3-photon process), and ~ 1.5 MW/cm^2 for coated $LiNbO_3$ at 532 nm (2-photon process) are required, well below the damage limits of the materials. The intensity required for the multiphoton process in $LiNbO_3$ is not high enough for thermionic emission to be noticeable. For comparison, the intensity required to use the linear emission produced by 532 nm illumination of cesiated, coated $LiNbO_3$ is ~ 10 W/cm^2, based on the quantum yield of 3×10^{-5} electrons/photon.

The current density needed to provide a directly viewable image of the quality predicted by eq. 3-1 would be obtained by taking

$T \approx 0.1$ second, the response time of the eye. Such an image is needed to adjust the sample position and the electron optics. Fortunately a suitable image can be obtained by illuminating the sample surface with ultraviolet and utilizing the ordinary linear photoemsiion to make the adjustments. The linear photocurrent normally will be much larger than the nonlinear response induced by the evanescent wave. Ultraviolet laser sources for use in photoelectron microscopy of high work function materials have been developed[36,37,38] and can provide resolution better than 1000 Å. These focusing illuminators will be discussed in more detail in Chapter 4.

The considerations above determine the minimum current densities required for high resolution imaging. The peak current densities required by such arguments cannot, in any case, exceed the space charge limit given by Child's Law[39]

$$J = 2.33 \times 10^{-6} \, V^{3/2}/d^2 \ \mathrm{amp/m^2} \qquad (3\text{-}2)$$

where V = applied voltage and d = anode-cathode separation in meters. Emission saturation due to space charge sets an absolute upper bound to the current densities, but beam current dependent aberrations will certainly be introduced at current densities well below the limit computed from Child's Law. A typical high resolution photoelectron microscope has an anode-cathode distance of 4 mm and an acceleration potential of 30 kV, corresponding to a maximum emission of 75 $\mathrm{A/cm^2}$ according to eq. 3-2. The peak current density required by the flash pumped laser is .2% of this and is probably too high to be useful, while the continuously pumped laser has a peak current density of only .0002% of the Child's Law maximum and space charge effects in that case would be inconsequential.

3.2. Sample Conductivity and Sample Charging

Artifacts due to the accumulation of charge on the surfaces of poorly conducting samples are well known in electron microscopy. Many methods have been devised to eliminate these charging artifacts, including the use of various coating materials, ultraviolet induced photoconductivity, sample heating, and the use of differential pumping to allow the specimen under examination to be maintained in a vacuum of only a few Pa of water vapor.[40,41]

The bulk conductivity required for successful imaging in conventional photoelectron microscopy has been estimated by Weber and Oswald[42] to be $\sigma \sim 10^{-8}\ \Omega^{-1}\ \text{cm}^{-1}$. This value is adequate for continuous illumination but for pulsed light sources should be increased to about $10^{-6}\ \Omega^{-1}\ \text{cm}^{-1}$ for the duty factor associated with the continuously pumped laser. The value of conductivity required may be understood by using the standard result for charge relaxation in a conductor.[43] The free charge density ρ decays according to

$$\rho = \rho_0\, e^{-t/\tau_R} \qquad (3\text{-}3)$$

where $\tau_R = \varepsilon_r \varepsilon_0/\sigma$. If charging is to be avoided during pulses of 100 ns duration, τ_R is required to be less than about 10 ns. For $\tau_R = 10$ ns and $\varepsilon_r = 10$, $\sigma \sim 10^{-5}\ \Omega^{-1}\ \text{cm}^{-1}$ (for GaAs, $\varepsilon_r \sim 13$ and for

$LiNbO_3$ $\varepsilon_r \sim 30$-80). Typical room temperature metallic conductivities are $\sim 10^5\ \Omega^{-1}\ cm^{-1}$, intrinsic silicon has $\sigma \sim 10^{-5}\ \Omega^{-1}\ cm^{-1}$, and plate glass has a value of $\sim 10^{-14}\ \Omega^{-1}\ cm^{-1}$. Therefore, only samples which are good insulators will produce sample charging artifact . The GaAs samples used for this dissertation have conductivity of $3 \times 10^{-9}\ \Omega^{-1}\ cm^{-1}$ and are not prone to serious charging artifacts. $LiNbO_3$, on the other hand, is an excellent insulator ($\alpha \sim 10^{-15}\ \Omega^{-1}\ cm^{-1}$) whose high high resistance properties have been used in a number of applications.[44] Therefore it was necessary to find a suitable method to prevent charge accumulation on $LiNbO_3$, without altering the guided or evanescent wave intensities to be examined. Two different approaches were tried:

1. Ultraviolet induced photoconductivity, and
2. Sample coating.

Sample coating proved to be the successful method but experiments involving both approaches are described below. Photoconductivity is the preferred method of charge relaxation as it does not alter the sample surface.

The average photoconductance induced in an insulating sample is given by[45]

$$\Delta g = eQ\mu\tau/L^2 \quad \text{in } \Omega^{-1} \tag{3-4}$$

where Q = carrier generation rate, μ = carrier mobility, τ = carrier lifetime, and L = sample length. This relationship holds for pulsed as well as continuous illumination provided that the pulse frequency is much less than the carrier lifetime. In the experiments done here Δg was measured and then the generation rate Q required to maintain the desired conductivity could be determined.

The initial attempt to measure the photoconductance on a $LiNbO_3$ sample used an electro-optic technique for measuring the photocurrent.[44] The experimental arrangement is shown in Figure 3-1. As used in this experiment, the $LiNbO_3$ electro-optic crystal was observed to discharge with a time constant of 40 seconds. The system capacitance was ~ 20 pF implying a minimum detectable current of 5×10^{-10} A. Laser beams of average powers of near 1 mw at wavelengths of 355 nm, 266 nm, and 219 nm were used on a $LiNbO_3$ sample crystal but in no case was any photocurrent detected. The carrier lifetime τ and bulk photoconductivity may be estimated if the mobility μ is assumed to be ~ 100 $cm^2/V/sec$. Since $(\Delta g)^{-1} > 10^3 \, V/(5 \times 10^{-10})A = 2 \times 10^{12} \, \Omega$ and the sample dimensions were .5 cm × .5 cm × .1 cm, the induced photoconductivity $\Delta\alpha < 5 \times 10^{-12} \, \Omega^{-1} \, cm^{-1}$. The carrier lifetime may be determined from eq. (3-4) by rewriting as

$$\tau = \Delta g L^2 / e \mu Q. \tag{3-5}$$

Then $\tau < 5 \times 10^{-12}$ seconds.

Another photoconductivity experiment was carried out using an Oriel 150 watt xenon arc lamp and a Keithley Model 410 micromicroammeter. The sample was the same as used above. The arc power absorbed by the $LiNbO_3$ crystal was ~ 20 mw and was at wavelengths below ~ 360 nm. This optical power produced a current of 4.5×10^{-12} A in the sample, with the sample biased at 1000 V. If the

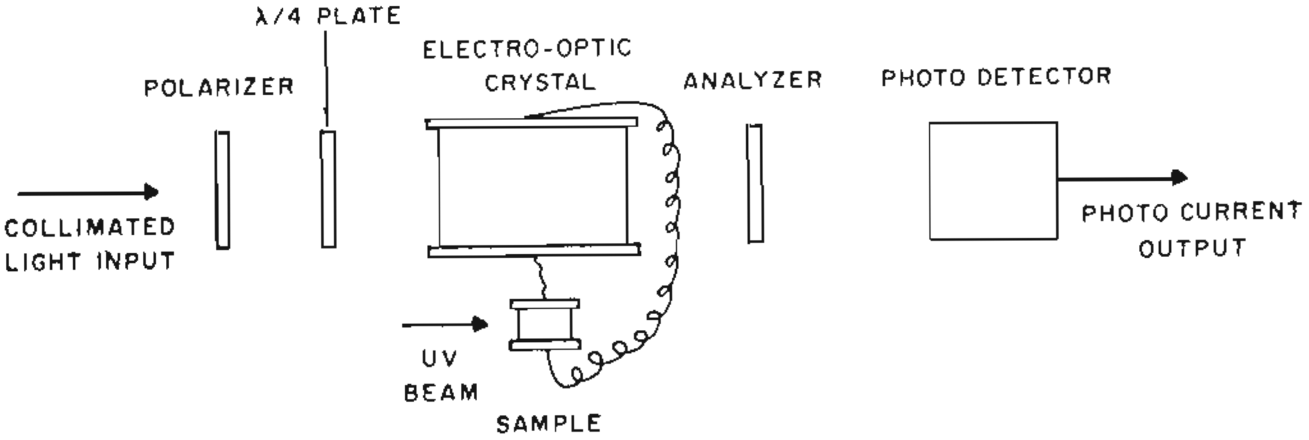

Figure 3-1. Electro-optic technique for the measurement of $LiNbO_3$ photoconductivity.

average photon energy is assumed to be 4 eV, the induced conductivity may be obtained as before. The results are $\Delta\sigma \sim 5 \times 10^{-14}$ Ω^{-1} cm^{-1} and $\tau \sim 5 \times 10^{-14}$ seconds.

Given the value of the carrier lifetime, the average ultraviolet power required to generate the needed photoconductivity can be calculated. The induced photoconductivity in a sample of dimensions $L \times L \times t$ (where t is thickness in which the ultraviolet power is to be absorbed) is $\Delta\sigma = L\Delta g/Lt = eQ\mu\tau/L^2t$. Therefore, the required generation rate $Q = L^2t\Delta\sigma/e\mu\tau$. In terms of average ultraviolet intensity, $Q = IL^2/e\hbar\omega$. Therefore,

$$I = \hbar\omega t\Delta\sigma/\mu\tau \qquad (3\text{-}6)$$

For $\Delta\sigma = 10^{-8}$ Ω^{-1} cm^{-1} in a layer of thickness 1 μm induced by 4 eV photons, $I = .8\text{W/cm}^2$. A typical sample is about .1 cm × .1 cm and an average ultraviolet power of 8 mW is required.

A less elegant, but simpler procedure for dealing with surface charging is to coat the sample with a thin conducting layer. The requirements for the coating, in addition to its properties as a conductor, are that it should be optically thin so that optical fields in the substrate will penetrate through the film, and that the coating be capable of withstanding laser pulse intensities of ~ 10 MW/cm^2.

Several materials were evaluated for coating. A sputtered gold-palladium coating commonly used in SEM was tried, but it was found to damage at laser intensities below 1 MW/cm^2. An evaporated antimony coating was also tried, but coatings thick enough to produce a low surface resistance transmitted only 10% of the visible light incident. The material eventually selected was tungsten, applied by heating a .25 mm filament held a few centimeters from the sample and heated to a temperature of 3000 K for a few minutes. This treatment forms a layer of resistance ~ 100 kΩ on the .5 cm × .5 cm face of the sample and decreased the optical transmission of the sample by less than 10%.

The thickness of the tungsten layer as well as that of the cesium coatings used to reduce the sample work functions was measured by two different methods. First, a gravimetric method was used. A preweighed 47 mm Nucleopore filter (mass ~ 15 mg) was exposed to the coating material under the appropriate conditions. Its mass increase was then measured on a Cahn 25 Automatic Electrobalance (sensitivity ~ 10 μg). The coating thickness was calculated by assuming an approximate area over which the coating was distributed and using the relation[46]

$$T = \frac{\mu g/cm^2}{\rho} \times 100\ \text{Å} \qquad (3\text{-}7)$$

where T = thickness and ρ = density in g/cm^2. To verify these measurements, the amount of material deposited per unit area was measured by x-ray fluorescence on an Ortec TEFA. The x-ray fluorescence technique is sensitive only to the individual atomic species selected and is calibrated against standards of known mass/area. The results of these measurements for both tungsten and cesium coatings are shown in Table 3-1. The data indicate coating thickness very much less than optical wavelengths so that evanescent waves can be expected to penetrate these surface layers.

3.3. Aberrations

The application of photoelectron microscopy to the imaging of nonlinear photoemission may require the use of pulsed optical beams and the peak photocurrent densities generated by these beams will be higher than the average values needed to obtain adequate image resolution with exposures of reasonable duration as discussed in section 3-1. The resolution of the electron microscope can be reduced by the presence of space charge in the electron path. In this section, the aberrations introduced by the use of high current density beams will be evaluated. As a function of current density, these aberrations can be divided into two groups: those that depend on the mean charge density; and those that depend on density fluctuations present because of the discrete electronic charge. The former effects will be referred to as "deterministic" and the latter as "statistical." Some of these effects alter the trajectories of electrons so that their apparent origin is unchanged, while others leave the origin unchanged but alter the energy or position of the particle at the electron objective lens so that chromatic or spherical aberrations of the lens are increased. Accordingly, the formulae for spherical

TABLE 3-1

COATING THICKNESSES

Coating Material	Measurement Technique	
	Gravimetric	X-ray
Cs	1200 Å	400 Å
W	< 200 Å	< 10 Å

and chromatic aberrations will be presented first and then the current density dependent aberrations will be discussed. Finally, the aberrations will be compared for a typical value of current density.

Throughout this analysis we make the following approximations and assumptions:

1. The electron velocities are nonrelativistic, and the significant forces are electrostatic;

2. The dominant aberrations are introduced in the space between the sample and objective lens, or by that lens itself, but not by other elements or spaces in the electron optical column;

3. The probability of electron emission is uniform in time and uniform in position within a circular illuminated region on a planar sample;

4. The alterations in trajectories are small compared to the electron beam diameter or field of view of the microscope.

The first approximation is valid for typical imaging systems with anode potentials near 30 kV. Approximation (2) is justified for systems using objective lenses of short focal length with a large magnification in the first imaging stage. Approximation (3) restricts the analysis to cases in which the current pulse duration is long compared to the time required for the particles to move through an appreciable portion of the electron optical system. Usually the electrons will travel from the sample to the anode or objective lens in about 100 picoseconds; hence this is not a severe limitation in most cases. Similarly, the assumed uniform emission distribution is valid if the mean electron separation is so large that the potential energy of a pair is small compared to energy available in the emission process. With an accelerating field of 75 kV/cm and current densities below 10 A/cm^2 the expected separation between an electron just leaving the cathode and its nearest neighbor will be above 1 μm, which corresponds to 1.4×10^{-3} eV, much less than the photon energy. The last assumption (4) depends on the beam diameter, of course, but should be valid in any optical system that yields many resolvable image elements within its field of view.

Other approximations have also been made in the treatment of specific cases, as discussed below.

3.3.a. Spherical and Chromatic Aberration

The formulae for both spherical and chromatic aberration can be found in the standard works on electron optics.[47,48] The chromatic image blur radius can be estimated from

$$h_c = C_c \alpha (\Delta W / e\phi_a) \qquad (3\text{-}8)$$

where C_c is the chromatic aberration coefficient of the lens, α is the aperture half angle subtended at the sample, and ΔW is the energy spread in the beam. For a typical electrostatic lens used in microscopy $C_c \approx 4f \approx 28$ mm (where f is the focal length) and $\alpha = 10^{-2}$, which result in an aberration blur radius $h_c = 93$ Å for a 1 eV initial energy spread in a 30 kV electron beam.

The spherical aberration can be evaluated from the formula

$$h_s = \tfrac{1}{4} C_s \alpha^3 \qquad (3\text{-}9)$$

where the spherical aberration coefficient C_s is about ten times the focal length for electrostatic lenses. The typical electrostatic objective lens will have $C_s \approx 70$ mm giving an aberration h_s of about 175 Å.

3.3.b. Deterministic Aberrations

The electron optical system configuration used in photoelectron microscopy consists of a planar sample illuminated over a diameter $2\ r_0$ and facing a planar accelerating electrode (anode) located at the front of the objective lens of the microscope. A hold in the anode permits the electrons to pass into the rest of the optical system. Typically the anode potential ϕ_a is about 30 kV with respect to the sample, and the spacing D is about 4 mm, giving an accelerating field of 75 kV/cm.

In the deterministic model we assume that a continuous charge density fills the beam as a result of the average photoelectron current density. Because we assume that any spreading of the electron beam is small compared to r_0, the current density $J = I/\pi r_0{}^2$ does not vary along the beam axis. The influence of space charge on the axial electron velocity is taken to be small; i.e., the time and position of the particle are related by

$$t = (2mDz'/e\phi_a)^{1/2} \tag{3-10}$$

where m and e are the electronic mass and charge. In this model both the radial and axial components of the space charge field produce trajectory shifts which change the apparent position of the sample.

It is easy to show that, in the absence of space charge, electrons leaving the sample with very small initial velocities travel in parabolic trajectories which intersect the anode plane at such positions R_0 and angles θ_0 (see Figure 3-2) that they appear to originate at a virtual image plane located a distance 2D in front of the anode. Each virtual source point is at the same position (shown by the dashed line) relative to the beam axis as the true source, but it is twice as far from the anode as the true source. The radial space charge held increases the radial velocity and the radius at which the electron crosses the anode plane; the axial space charge field changes only the position at which the electron crosses the anode plane due to the increased time of flight which the electron experiences as a result of space charge.

The aberrations introduced by the radial component of the space charge field have been analyzed by Plummer.[49] He numerically evaluated the radial electric field at the edge of an electron beam in a uniform accelerating field and integrated the equations of motion to find the radial position and velocity shifts. Referring to Figure 3-2

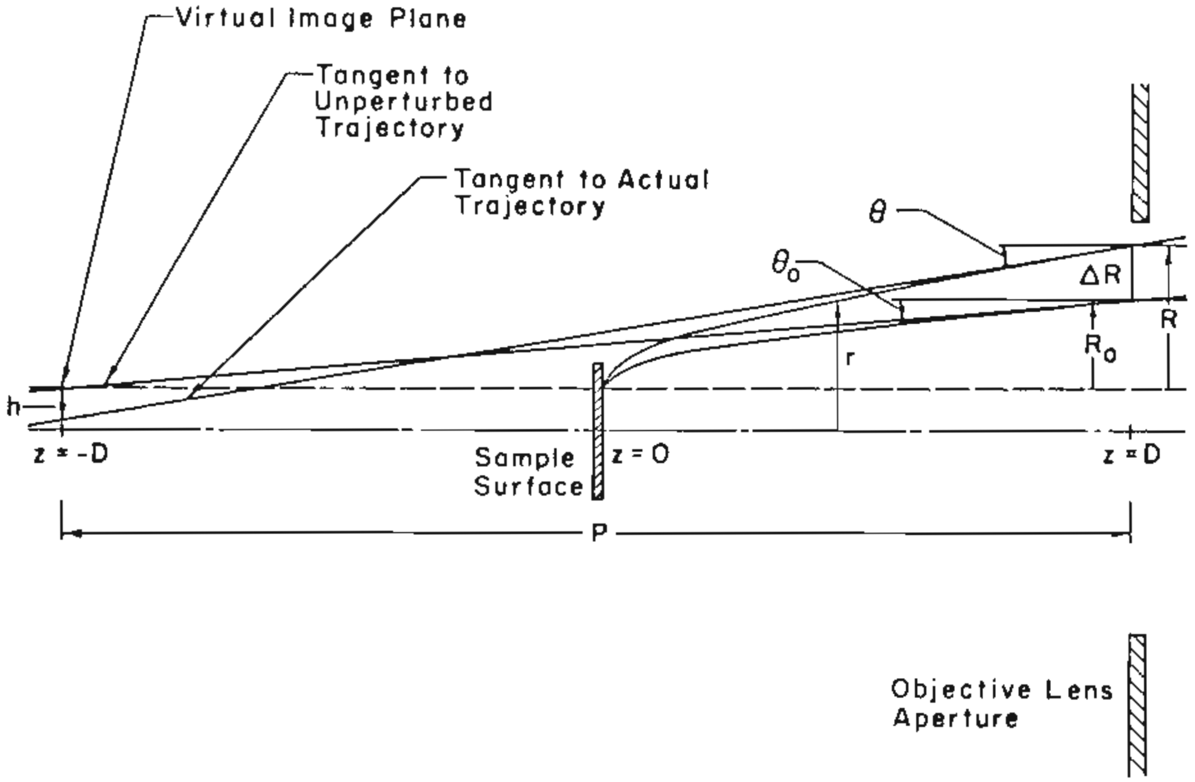

Figure 3-2. Diode region of the photoelectron microscope. Aperture is at potential ϕ_a relative to sample. Transverse dimensions and beam spreading are exaggerated.

and assuming that the initial electron velocity is small, it follows from the geometric relation

$$\tan\theta = (h + R_0 + \Delta R)/2D \tag{3-11}$$

that

$$h = \Delta v_r D(2m/e\phi_a)^{1/2} - \Delta R. \tag{3-12}$$

Plummer used eq. (3-12) together with numerical evaluation of Δv_r and ΔR to obtain h. He thus showed that the Gauss's Law approximation for the field gave a result which preducts aberrations within a few percent of the exact values. The final result for the aberration (using the Gauss's Law approximation) is

$$h(r) \approx (JrD^2/\varepsilon_0\phi_a{}^{3/2})(m/2e)^{1/2}. \tag{3-13}$$

Because h is not a function of v_{r0}, this deterministic space charge effect is not one of the usual aperture-dependent optical aberrations. Recalling that r is the distance from the true object point to the optical axis (or center of field of view), we see that the linear r dependence in h implies a simple demagnification by the factor (r-h)/r. Every point in the image moves toward the axis as J increases during the current pulse, producing a radial image blur. If continuous illumination were used this effect would be insignificant.

The axial component of the space charge field also produces a weak trajectory aberration, by altering the electron's time of flight to the anode plane so that it reaches the anode at a height different than that in the unperturbed case. There is no change in either component of electron velocity.

The results of Plummer's numerical evaluation of $E_z(r = 0, z)$[50] may be used to find the time of flight to the anode in the presence of space charge. The anode-cathode distance is divided in small increments $\Delta z_{i+1} = z_{i+1} - z_i$. The work done by the fields (both the static accelerating field and the current density dependent field) on the electron as it passes through Δz_{i+1} is $W = eE_z \Delta z_{i+1}$ and from conservation of energy we find that the z component of the electron's velocity at z_{i+1} is

$$\dot{z}_{i+1} = [(2e/m)E_z(z_{i+1} - z_i) - \dot{z}_i^{\,2}]^{1/2}. \tag{3-14}$$

The time of flight may be found by assuming that the average electron speed in Δz_{i+1} is $(\dot{z}_i + \dot{z}_{i+1})/2$ and, therefore, the total time of flight is

$$t = 2\sum (z_{i+1} - z_i)/(\dot{z}_{i+1} + \dot{z}_i). \tag{3-15}$$

The time of flight was evaluated numerically for the values of perturbing field found in Table 3-2 and for 10, 100, and 1000 times these values, using a computer program listed in Appendix 1. The results of the time of flight calculations are found in Table 3-3. These data may be used to find the approximate scaling for the ratio $\Delta t/t_0$, where Δt is the change in time of flight, and t_0 is the unperturbed time of flight.

TABLE 3-2

LONGITUDINAL COMPONENT OF THE DETERMINISTIC SPACE CHARGE INDUCED ELECTRIC FIELD AS A FUNCTION OF z

$z(\mu m)$	$E_z(0,z)$ (V/cm)
0.0	-25.49
0.1	-22.23
1.0	-16.38
2.0	-10.53
3.0	- 6.94
4.0	- 5.06
5.0	- 3.18
10	- 0.47
15	- 0.08
20	0.22
25	0.25
30	0.26
40	0.23
50	0.20
100	0.10
300	0.03
500	0.02
1000	0.01
2000	0
4000	0

TABLE 3-3

TIME OF FLIGHT ALTERATION: DETERMINISTIC E_z*

Current Density A/cm^2	Time of Flight psec	$\Delta t/t_o$
0.0	77.8755	---
1.27	77.8760	6.4×10^{-6}
12.7	77.8883	6.2×10^{-5}
127	77.9240	6.2×10^{-4}
1270	78.4189	7.0×10^{-3}

*t_o is the time of flight in the absence of space charge. Data are for $\phi_a = 30$ kV, D = 4 mm, and $r_o = 5$ μm.

It may be shown that the deterministic $E_z(0, z)$ of Table 3-2 is given by

$$E_z(0, z) = (4\pi\varepsilon_0)^{-1} (2mD/e\phi)^{1/2} Jr_0 \, G(z/r_0)$$

where

$$G(z/r_0) = \pi \int_0^{D/r_0} dw' \int_0^1 \rho' d\rho' \left\{ \frac{(z/r_0 - w')}{[(z/r_0 - w')^2 + \rho'^2]^{1/2}} - \frac{(z/r_0 + w')}{[(z/r_0 + w')^2 + \rho'^2]^{1/2}} \right\} w'^{-1/2}$$

Using the fact that $\Delta t/t_0$ varies linearly with the strength of the perturbing field, we obtain the result

$$\Delta t/t_0 = 9.04 \times 10^{-6} (4\pi\varepsilon_0)^{-1} (2mD/e\phi_a)^{1/2} Jr_0 .$$

Referring to Figure 3-2 we see that the apparent origin of the electron is at a distance P from the anode and

$$P = h(v_{zf}/v_r) \tag{3-16}$$

with $v_{zf} = (2e\phi_a/m)^{1/2}$. Using the delayed time of flight, the apparent object position is

$$P = v_r(t_0 + \Delta t)(v_{zf}/v_r) \tag{3-17}$$

$$= 2D(1 + \Delta t/t_0). \tag{3-18}$$

The lateral blur associated with this shift is

$$h_{E_z} = (\alpha/2)\ 2D(\Delta t/t_0)$$

$$h_{E_z} = 9.04 \times 10^{-6}\ \alpha(4\pi\ _0)^{-1}\ (2mD^2/e\phi_a)^{1/2}\ Jr_0. \qquad (3\text{-}19)$$

For $J = 1$ A/cm^2, $\alpha = 10^{-2}$, $D = 4$ mm, $\phi_a = 30$ kV, $r_0 = 5$ μm, $h_{E_z} \sim 2$ Å.

3.3.c. Statistical Aberrations

The linear dependence of h on J in the above treatment suggests that eq. 3-13 might underestimate the aberration for small currents, in which case effects related to shot noise in the beam might be expected to become significant. This problem is related to the energy broadening process known as the "Boersch effect," which has been observed and analyzed by a number of investigators.[51-57]

Previous treatments of energy spreading have been concerned with thermionic or field emission electron sources, and they have concentrated on the redistribution of thermal velocities through collisions between electrons during their time of flight. When laser-induced photoemission is the generating mechanism, the initial electron kinetic energy spread can vary over a much wider range, because the photon energy is much larger than kT for a typical thermionic electron source, yet the photons are essentially monochromatic and the emitter temperature is much lower than that of a thermionic source yeilding the same current density. We therefore treat initial velocity effects separately from the image blurring mechanisms related to the initial potential energy of the local electron configuration. The former depend on the light wavelength, photoelectric threshold, and sample temperature, while the latter depend on the beam current density.

In dealing with the potential energy relaxation we assume that photoemission occurs strictly with Poisson statistics (equal likelihood of emission from equal areas within the illuminated spot on the cathode, and equal likelihood of emission in equal times from each point in the spot). This process introduces a random potential energy into the beam, and as the particles move under these repulsive forces, kinetic energy fluctuations appear at the anode, reducing the image quality through the chromatic aberration coefficient of the microscope objective lens.

We begin by computing the mean square fluctuation in the longitudinal electric field component at a point on the axis of a long electron beam of radius r_0. In cylindrical coordinates (θ,r,z) centered on the field point at a distance Z from the cathode, this can be written as

$$\langle E_z^2(r=0,z=0,Z)\rangle$$

$$= \left(1/4\pi\epsilon_o\right)^2 \left\langle \left[\int_{\theta=0}^{2\pi}\int_{r=0}^{r_o}\int_{z=-\infty}^{\infty} \rho(\overline{r})\,zr(z^2+r^2)^{-3/2}\,d\theta dr dz\right]^2 \right\rangle \qquad (3\text{-}20)$$

where $\rho(\overline{r})$ is the charge density at position $\overline{r}$, which is at $(\theta, r, z+Z)$. We make the approximation that $\langle\rho(\overline{r})\rangle$ varies slowly along the beam, and we note that the charge at $|z| >> r_o$ produces a very small effect so that the infinite limits can be retained but image charges can be omitted. Then converting from ρ to electron number density n using $\rho = -en$ and inverting the order of multiplication and summation, we obtain

$$\langle E_z{}^2\rangle = \int_{\theta'=0}^{2\pi} \int_{\theta''=0}^{2\pi} \int_{r'=0}^{r_o} \int_{r''=0}^{r_o} \int_{z'=-\infty}^{\infty} \int_{z''=-\infty}^{\infty} F(\overline{r})\,d\theta'\,d\theta''\,dr'\,dr''\,dz'\,dz'' \tag{3-21}$$

where

$$F(\overline{r}) = \left(e/4\pi\epsilon_o\right)^2 \langle n(\overline{r'})n(\overline{r''})\rangle\, r'\,r''\,z'\,z''\left(z'^2 + r'^2\right)^{-3/2}\left(z''^2 + r''^2\right)^{-3/2}. \tag{3-22}$$

For uniformly distributed points in three dimensions, it is easily shown[58] that

$$\langle n(\overline{r'})n(\overline{r''})\rangle = \langle n\rangle^2 + \langle n\rangle\delta(\overline{r'} - \overline{r''}) \tag{3-23}$$

where $\langle n\rangle$ is the mean value of n over the region of interest and $\delta(\overline{r'} - \overline{r''})$ is the three dimensional Dirac delta function. Applying eqs. 3-23 and 3-22 to eq. 3-21, we note that the first term in eq. 3-23 contributes nothing because of the odd symmetry of its integrand about $z = 0$, and the sampling property of $\delta(\overline{r})$ yields

$$\langle E_z{}^2\rangle = 2\pi\left(e/4\pi\epsilon_o\right)^2 \int_{z=-\infty}^{\infty} \int_{r=0}^{r_o} \langle n\rangle z^2 r(z^2 + r^2)^{-3} dr dz$$

$$\approx 4\pi\left(e/4\pi\epsilon_o\right)^2 \int_{z=0}^{\infty} \int_{r=0}^{r_o} \langle n\rangle z^2 r(z^2 + r^2)^{-3} dr dz \ . \qquad (3\text{-}24)$$

At this point we note that if <n> were a constant, the integral would diverge. In fact, however, the electrons in the beam are accelerating uniformly, so that <n> varies slowly with distance from the cathode according to

$$\langle n(Z)\rangle = J\ e^{-3/2}\ \left(mD/2Z\phi_a\right)^{1/2} \qquad (3\text{-}25)$$

using the notation of Section 3.3.b. above. In addition, we really want to evaluate $\langle E_z{}^2\rangle$ at the site of a typical moving electron located at (r = 0, Z). Thus we note that for Z > 0 the value of <n> must be zero in the immediate vicinity of this electron, because Coulomb repulsion will have moved any closely-spaced electron pairs apart by some distance s before they reach Z. A modified spatial distribution function therefore exists at small (r, z), and the modification increases with Z. We take this potential relaxation into account by replacing the inner (zero) limits on r and z in eq. 3-24 by a variable distance s(Z), which gives

$$\begin{aligned}\langle E_z{}^2(Z)\rangle &= (\pi/2)\left(e/4\pi\epsilon_o\right)^2 \langle n\rangle \Big[1/2s - s/\left(s^2 + r_o{}^2\right) \\ &\qquad + \pi/4s - \pi/2r_o + \left(1/r_o\right) \tan^{-1}\left(s/r_o\right)\Big] \\ &\approx K_1 \left(e/4\pi\epsilon_o\right)^2 \langle n(Z)\rangle/s(Z) \end{aligned} \qquad (3\text{-}26)$$

when $s(Z) << r_0$. The constant K_1 is $(\pi/4)(1 + \pi/2)$ for a cylindrical boundary. If instead we had integrated down to a spherical inner limit of radius $s(Z)$ centered on $(r = 0, Z)$, a more symmetrical choice, we would obtain the slightly different value

$$K_1 = 4\pi/3. \qquad (3\text{-}27)$$

A similar result has been given by DeChambost and Hennion[56] based on different reasoning. We note that the assumption of slowly varying $\langle n\rangle$ was used to obtain eq. 3-26.

In the cases of interest here, $s << n^{-1/3}$, so that the relaxation motions generally occur between isolated pairs of electrons that happen to be unusually close together. Since the outside accelerating force $e\ \phi_a/D$ acts equally on both members of the pair, they separate according to the same relative equation of motion as if the outside forces were removed. This problem is easily solved;[59] at a time t after leaving the cathode, a pair originally separated by s_0 will be separated by s, as given by

$$\begin{aligned} &t\ s_o{}^{-3/2} \left(e^2/\pi\epsilon_o m\right)^{1/2} \\ &= (x^2-x)^{1/2} + 1/2\ \ell n\left[2(x^2-x)^{1/2} + 2x - 1\right] \end{aligned} \qquad (3\text{-}28)$$

where $x = s/s_0$ and $t = (2m\ Z\ D/e\phi_a)^{1/2}$.

We can now evaluate $<E_z{}^2>$ at Z using eqs. 3-25 through 3-27 by inserting the appropriate limit s for that position, based on eq. 3-28. Specifically, we associate with each Z (or t) that s_0 value for which $s/s_0 = x = 2$; i.e., we cut off the spatial probability distribution at such an inner range that half or more of the potential energy of the eliminated electron pairs has already been converted to kinetic energy by the time the pair reaches that position. For that choice

$$s(Z) = 2\left(2eD\ Z/\pi K_2^2\ \epsilon_o\phi_a\right)^{1/3} \tag{3-29}$$

$$\text{where } K_2 = \sqrt{2} + 1/2\ \ell n\ (2\sqrt{2} + 3)\ . \tag{3-30}$$

We therefore obtain the rms field fluctuation $\delta E_z = <E_z{}^2>^{1/2}$ from Eqns.(21) and (24):

$$\delta E_z(Z) = K_1{}^{1/2}\ K_2{}^{1/3}\ 2^{-35/12}\ \left(\pi\epsilon_o\right)^{-5/6}\ m^{1/4}\ J^{1/2}\left(eD/\phi_a Z^5\right)^{1/12}. \tag{3-31}$$

The energy spread ΔW_a at the anode can be found simply by integrating the force $e\delta E_z$ along Z:

$$\Delta W_a = e\int_{Z=0}^{D} \delta E_z(Z)dZ$$

$$= (3/7)\ 2^{-11/12}\ K_1{}^{1/2}\ K_2{}^{1/3}\ (\pi\epsilon_o)^{-5/6}\ e^{13/12}\ m^{1/4}\ D^{2/3}\ J^{1/2}\ \phi_a{}^{-1/12}. \tag{3-32}$$

In setting up the uniform random space charge distribution at the cathode that eventually led to ΔW above, we did not place any bound such as the thermal energy kT or the photon energy $h\nu$, on the available potential energy. The very close pairs are so unlikely and their force is exerted over such a short relaxation distance that the net energy spread converges without any energy-limiting assumption. Although our arbitrary choice of $x = 2$ in selecting s tends to make eq. 3-32 underestimate the total spread, the error is less than a factor of two, because most of the charge pairs release less than half their potential energy before they reach the anode, and such pairs are not affected by the truncation of δE at $s(Z)$ given by eq. 3-29.

When the beam width is sufficiently large that the field fluctuations are reasonably isotropic near the axis, one can also use eq. 3-31 to describe the transverse fluctuations δE_r produced by the random charge density. The radial equation of motion

$$d^2r/dt^2 = e\delta E_r/m \tag{3-33}$$

can be integrated by transforming t to Z, and the rms values of velocity δv_r and position δR can be obtained:

$$\delta v_r(Z) = (3/2)\ K_1{}^{1/2}\ K_2{}^{1/3}\ \left(\pi\epsilon_o\right)^{-5/6}\ m^{1/4}\ J^{1/2}\ \left(eD/\phi_a\right)^{7/12}\ Z^{1/12}; \tag{3-34}$$

$$\delta R(Z) = (9/7)\ 2^{1/12}\ K_1{}^{1/2}\ K_2{}^{1/3}\ \left(\pi\epsilon_o\right)^{-5/6}\ m^{1/4}\ e^{1/12}\ J^{1/2} \times \left(D/\phi_a\right)^{13/12}\ Z^{1/12}. \tag{3-35}$$

To estimate the magnitudes of ΔW_a and h_t we evaluate eqs. 3-32 and 3-36 for the case $\phi_a = 3 \times 10^4$ volt, D = 4 mm, and J = 1 A/cm^2. We obtain $\Delta W_a = 5.5 \times 10^{-20}$ joule or 0.34 eV, a reasonable value. The corresponding chromatic image blur radius can be evaluated from eq. 3-8 and the result is $h_c = 32$ Å. Now if h_t is evaluated using eq. 3-36, given the same parameters, we obtain $h_t = 458$ Å, a much larger effect. Evidently the transverse random field fluctuations are more significant than the longitudinal ones.

The rms field fluctuation δE_z also produces a time of flight trajectory aberration in the same fashion in which the deterministic E_z caused an image blur. Computer evaluations of $\Delta t/t_0$ were performed for various values of the perturbing δE_z field. The results are in Table 3-4 and the computer program is in Appendix A2. When the appropriate scaling factors are introduced, we find that

$$h_{\delta E_z} = 3.89 \times 10^{-6}\, K_1{}^{1/2}\, K_2{}^{1/3}\, 2^{-35/12}\, (\pi\varepsilon_0)^{-5/6}\, m^{1/4} \times J^{1/2}\, e^{1/12}\, D^{13/12}\, \phi_a{}^{-1/12}\, \alpha. \tag{3-37}$$

For J = 1 amp/cm^2 and the usual values for the other parameters, $h_{\delta E_z} \sim 8$ Å.

We now consider redistribution of initial kinetic energy by electron scattering in the accelerating beam. This energy may be present if the photon energy $h\nu$ substantially exceeds the photoelectric

TABLE 3-4

TIME OF FLIGHT ALTERATION: STATISTICAL E_z*

Current Density A/cm^2	Time of Flight psec	$\Delta t/t_o$
0.0	77.87545	---
1.0	77.87394	1.9×10^{-5}
1.0×10^2	77.86036	1.9×10^{-4}
1.0×10^4	77.72571	1.9×10^{-3}
1.0×10^6	76.47845	1.8×10^{-2}

*t_o is the time of flight in the absence of space charge. Data are for ϕ_a = 30 kV and D = 4 mm.

threshold energy for the sample, or it may be due to the thermal energy kT if the sample is heated. Although we may assume the initial velocity distribution is nearly isotropic, in the reference frame of the moving electrons the axial velocity spread almost vanishes after the beam is accelerated through a potential of a few tens of eV.[55] Collisions scatter the transverse energy into the axial direction as thermal equilibration takes place in the moving coordinate system. In the laboratory frame, however, this change in axial energy increases the total (rms) energy spread $\Delta W_T(Z)$ according to the relation

$$\Delta W_T^{\,2}(Z) = \Delta W_o^{\,2} + \int_0^Z \frac{d\left(\Delta W_s^{\,2}\right)}{dZ}\, dZ, \tag{3-38}$$

where W_0 is the mean square axial energy spread at the cathode, and $d(\Delta W_s^{\,2})/dZ$ is the rate of growth of mean square energy spread with distance from the cathode as a result of acattering. To evaluate the integral in eq. 3-38, we use the theory developed by Knauer[55] for the scattering rate in a beam moving at a given potential ϕ:

$$\frac{d\left(\Delta W_s^{\,2}\right)}{dZ} = 2^{-7/2}\, \pi^{-1/2}\, e^3\, \epsilon_o^{\,-2} \left(m/\Delta W_o\right)^{1/2} J \,\ln \Lambda \tag{3-39}$$

$$\text{where } \Lambda = 8\pi\, e^{-3/2}\, \epsilon_o\, \Delta W_o\, J^{-1/3}\, (2\phi/m)^{1/6}\ . \tag{3-40}$$

For electrons in a uniform field ϕ_a/D, the potential ϕ is $\phi_a Z/D$, so that

$$\Lambda = 8\pi\ e^{-3/2}\ \epsilon_o\ \Delta W_o\ J^{-1/3}\ \left(2\phi_a/mD\right)^{1/6}\ Z^{1/6}. \qquad (3\text{-}41)$$

We can therefore integrate eq. 3-39 over Z to obtain the mean square scattering contribution to eq. 3-38 at Z = D:

$$\int_0^D \frac{d\left(\Delta W_s{}^2\right)}{dZ}\, dZ = A(\ln B - 1/6) \qquad (3\text{-}42)$$

$$\text{where } A = 2^{-7/2}\ \pi^{-1/2}\ e^3\ \epsilon_o{}^{-2}\ \left(m/\Delta W_o\right)^{1/2}\ JD \qquad (3\text{-}43)$$

$$\text{and } B = 8\pi\ e^{-3/2}\ \epsilon_o\ \Delta W_o\ J^{-1/3}\ \left(2\phi_a/m\right)^{1/6}\ . \qquad (3\text{-}44)$$

Inspection of relations 3-38 and 3-42 through 3-44 shows that, although the total spread increases with ΔW_0, the fraction of ΔW_T contributed by relaxation grows smaller as the initial energy spread increases. For example, in a 1 A/cm^2 beam with ϕ_a = 30 kV and D = 4 mm, ΔW_T is 0.482 eV for ΔW_0 = 0.1 eV. Increasing ΔW_0 to 1.0 eV produces a total spread ΔW_T of 1.045 eV, almost all of which is the initial ΔW_0 component. Furthermore the dependence of ΔW_T on J and D is not a simple power-law relation, as it is for the other broadening mechanisms we have considered.

The magnitudes of these spreads indicate that the velocity relaxation mechanism produces an energy broadening comparable to that resulting from the potential energy relaxation, eq. 3-32.

Chromatic aberration blur radii of the order of 100 Å are therefore predicted for current densities in the 1 A/cm^2 range. If the initial energy spread is about 1 eV or greater, the statistical chromatic effects due to space charge at the usual current densities will be small compared to the chromatic aberration corresponding to the initial velocities alone. However, the trajectory blur h_t caused by the field fluctuations can be larger, reaching the 500 Å range at the higher current densities.

3.3.d. Aberration Summary

The chromatic, spherical, and image position aberrations of the initial diode region and objective lens portion of a photoelectron microscope have been analyzed. For comparison of the relative magnitude and parametric scaling factors of the various physical effects, Table 3-5 has been prepared. This table is appropriate for reasonably high-current, high-initial-velocity conditions encountered with laser illumination. The component aberrations add quadratically, giving a total rms blur radius of about 500 Å on the axis. It is clear that the trajectory alterations to the density fluctuations are the dominant effect.

Experiments performed with pulsed ultraviolet sources have shown the above effects. However, for current densities less than 1 A/cm^2 the aberrations still allow better than 500 Å resolutions. Even at 0.1 A/cm^2 the current density is far above the 1.6×10^{-8} A/cm^2

TABLE 3-5

ABERRATION SUMMARY

Aberration Type	Affecting Mechanism	Parametric Dependence[a]	Typical Magnitude[b]
Spherical	Angular spread	$C_s\alpha^3$	175 Å
Chromatic	Initial velocity	$C_c \Delta W_o \phi_a^{-1} \alpha$	93 Å
	Potential relaxation	$C_c J^{1/2} D^{2/3} \phi_a^{-1/12} \alpha$	32 Å
	Velocity relaxation[c]	$C_c J^{1/2} D^{1/2} \Delta W_o^{-1/4} \alpha$	28 Å
	Deterministic charge	0	0
Image Position (trajectory)	Deterministic charge (E_r)	$J D^2 \phi_a^{-3/2} r$	294 Å
	Density fluctuations (δE_r)	$J^{1/2} D^{5/3} \phi_a^{-13/12}$	458 Å
	Deterministic charge (E_a)	$J D r_o \phi_a^{-1/12} \alpha$	2 Å
	Density fluctuations (δE_z)	$J^{1/2} D^{13/12} \phi_a^{1/12} \alpha$	8 Å

[a] Note that α varies as $\Delta W_o^{1/2} \phi_a^{-1/2}$ if there is no stop.

[b] Computed for each component alone. Conditions: C_s = 70 mm, C_s = 28 mm, D = 4 mm, r = 5 μm, ΔW_o = 1 eV, ϕ_a = 30 kV, J = 1 A/cm^2, $\alpha = 10^{-2}$.

[c] Neglects slowly varying $\ell n \Lambda$ factor.

minimum value obtained from eq. (3-1). Lasers with relatively low duty factors can be used, therefore.

CHAPTER 4

PHOTOELECTRON IMAGING

This chapter describes photoelectron emission imaging experiments using both linear photoemission and the nonlinear processes of Chapter 2. Ultraviolet illumination is needed to provide linear photoemission in order to view the surface of the sample to be studied using nonlinear photoemission. It also provides the microscope operator with a simple means of focusing the instrument. The following sections summarize the requirements which must be met by suitable ultraviolet illuminators, and discuss in detail an ultraviolet source based on the optical harmonics of the continuously-pumped Nd:YAG laser. Electron micrographs obtained with the laser source will be presented.

4.1. Ultraviolet Source Requirements

The ultraviolet source requirements for photoelectron microscopy have been analyzed in detail by several workers.[60,61] The reasoning used is similar to that found in Section 3.2. One requires a minimum signal to noise ration per resolvable detail on the sample and thereby determines the minimum average current density. The result is eq. (3-1)

$$J_0 = e/\eta d^2C^2T. \qquad (3\text{-}1)$$

The current density is transformed into an average optical intensity via the photoelectric quantum yield (γ) and photon energy at the source wavelength ($h\nu$). Then,

$$I_0 = J_0(h\nu/\gamma) \tag{4-1}$$

or

$$I_0 = eh\nu/\gamma\eta d^2C^2T. \tag{4-2}$$

This is the basic relation which the ultraviolet intensity must satisfy. As a numerical example we use values similar to those of Chapter 3, i.e., $\eta = 0.1$, $d = 10^{-6}$ cm, $C = 0.1$, but take the exposure time to be 0.1 sec to match the response time of the eye. Then, according to eq. (3-1) the required current density is 1.6×10^{-3} A/cm^2. The photoelectric quantum yield is taken to be that of GaAs at 213 nm ($h\nu = 5.85$ eV), i.e., $\gamma = 5 \times 10^{-5}$. Then, from eq. (4-1), we obtain

$$I_0 = 190 \text{ watt/cm}^2.$$

For high magnification experiments the field of view of interest would be ~ 10 μm by 10 μm corresponding to an area of ~ 10^{-6} cm^2. The optical power required is thus 0.19 mW.

The ultraviolet wavelength needed depends on the photoemissive properties of the sample material but some general limits may be given. Sommer[62] lists the photoemission threshold wavelengths for a wide variety of metals and semiconductors. These values typically range from 4.5 eV to 6.0 eV, if the alkali metals are excluded. Thus, wavelengths in the range of 210-275 Å are required.

4.2. A Nd:YAG Based Ultraviolet Illuminator

There are many potentially useful coherent ultraviolet sources which satisfy the conditions of Section 4.1. If linear photoelectron microscopy were the only application of interest, noble gas ion lasers[63,64] and metal vapor lasers[65] would be suitable. The high duty factor of the metal vapor laser makes it the best available coherent ultraviolet source. For the application under consideration in this dissertation, however, linear emission is to be used only to map the sample surface and to focus the electron optics before viewing guided or evanescent waves propagating in the sample. Additional illumination in the visible or infrared is required for the nonlinear work. This makes an ultraviolet source based upon the Nd:YAG laser ideal, as this laser can provide two useful linear photoemission wavelengths (266 nm, 213 nm), two wavelengths appropriate for nonlinear photoemission studies (532 nm, 1064 nm) and can be used to pump a variety of dye lasers if radiation at additional wavelengths is needed. The source to be described here uses the Nd:YAG laser and a nonlinear converter which transforms a portion of the Nd:YAG 1064 nm fundamental to 266 nm in two frequency doubling steps and also produces the fifth harmonic (213 nm) by combining the 266 nm and 1064 nm radiation in a mixer crystal.[63,66] This nonlinear converter may be used with several different Nd:YAG laser configurations, depending on the duty factor desired.

The aberration considerations discussed earlier imply that a laser to be used with the above nonlinear process must have a reasonable duty factor. To illustrate this, three different Nd:YAG laser systems will be evaluated as ultraviolet sources based only on their duty factors. These laser systems are the flash-pumped, Q-switched laser, the intracavity-modulated burst mode laser, and the cw-pumped, repetitively Q-switched laser. The burst mode laser was developed to lower the peak powers of the flash-pumped laser while maintaining comparable average powers, and represents an intermediate between the flash-pumped and cw-pumped lasers. For a complete description of this laser, see reference 70. The duty factors of each of these lasers are presented in Table 4-1 along with the values of peak optical intensity and peak current density needed for successful use in imaging experiments. The successive improvement in duty factor is obvious. In addition, it can be shown that the intensities required of the flash-pumped and burst mode lasers can melt non-refractory samples.[67] The cw-pumped laser is clearly the best choice.

The cw-pumped Nd:YAG laser used in the nonlinear process mentioned above was pumped by two krypton arc lamps and Q-switched at kilohertz repetition frequencies by a conventional acoustooptic Bragg diffraction cell. A linear resonator configuration employing two plane mirrors was used, with a $LiIO_3$ harmonic generating crystal placed near one of the mirrors, which served as the output coupler. The $LiIO_3$ doubler was 1 cm long and antireflection coated for 1064 nm; it was oriented such that normal to the polished faces made an angle of ~ 30° with the crystalline optic axis.[68] A 1.4 nm aperture near the laser rod confined the mode order to TEM_{00}, and a fused

TABLE 4-1

PEAK CURRENT DENSITIES (J_o) AND OPTICAL INTENSITIES (I_o) REQUIRED BY THE IMAGING CONDITIONS OF 4.1. FOR VARIOUS Nd:YAG LASER CONFIGURATIONS

(Based on $\overline{I}_o = 200\ \mathrm{W/cm^2}$ and $\overline{J}_o = 1.6 \times 10^{-3}\ \mathrm{A/cm^2}$)

Laser Configuration	Repetition Rate	Pulse Length (nsec)	Duty Factor	I_o ($\mathrm{MW/cm^2}$)	J_o ($\mathrm{A/cm^2}$)
Flash-pumped	10 pulses/sec	5	5×10^{-7}	400	3×10^3
Burst Mode	10 bursts/sec × 10 pulses/burst	30	3×10^{-6}	70	5×10^2
cw-pumped	3000 pulses/sec	70	2×10^{-4}	1	8

silica Brewster plate was used to stabilize the 1064 nm polarization direction. Simultaneous output coupling for both the first and second harmonics was achieved using a mirror coating with 1.7 percent transmission at 1064 nm and 95 percent transmission at 532 nm.

Figure 4-1 shows the experimental configuration used to generate all the harmonics. A fused silica lens of 25 cm focal length was used to converge the laser output beams onto a 5 cm crystal of potassium dideuterium phosphate (KD*P, 99 percent deuterated) which served as the frequency doubler for the 532 nm/266 nm conversion process. The KD*P crystal was maintained at 42°C in a thermostatic oven. The beams leaving the KD*P doubler were refocused by a second fused silica lens (7.5 cm focal length) onto a 3 cm potassium dihydrogen phosphate (KDP) mixer crystal held at -40°C in a vacuum crystal.[69] All the nonlinear crystals were oriented for Type 1 phase matching.[70] The choice of KD*P was dictated by the requirements of providing 90° phase matching for doubling the 532 nm harmonic while providing minimum loss for the transmitted 1064 nm beams. KDP was used as the mixer because of its low loss, relative temperature insensitivity, and capability of providing 90° phase matching for sum generation with the 1064 and 266 nm harmonics. The various wavelengths leaving the mixer were separated by a fused silica prism.

Figure 4-2 indicates the average powers leaving the laser at 532 and 1064 nm as a function of Q-switch repetition frequency. The 1064 nm power indicated in the figure is the fraction polarized at

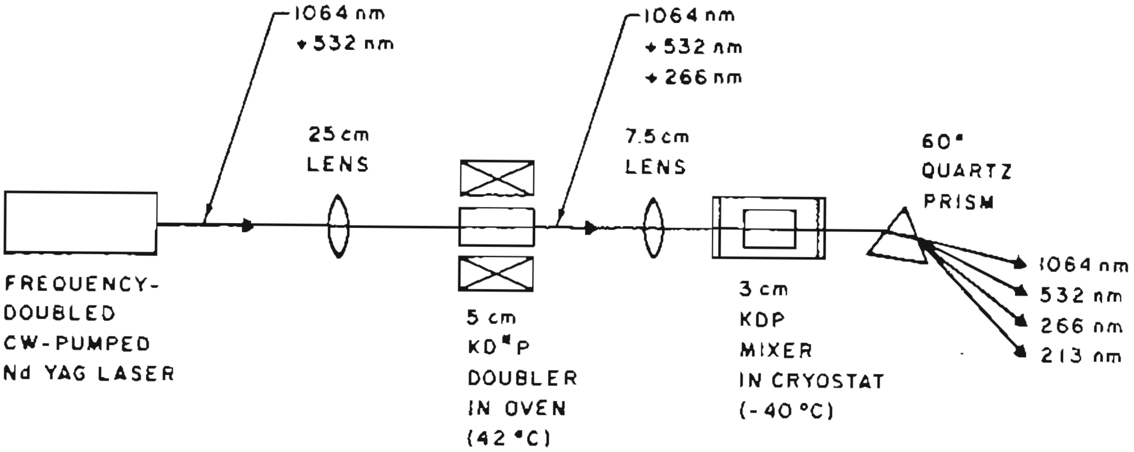

Figure 4-1. Apparatus for the collinear generation of the fourth and fifth harmonics of an internally frequency doubled Nd:YAG laser.

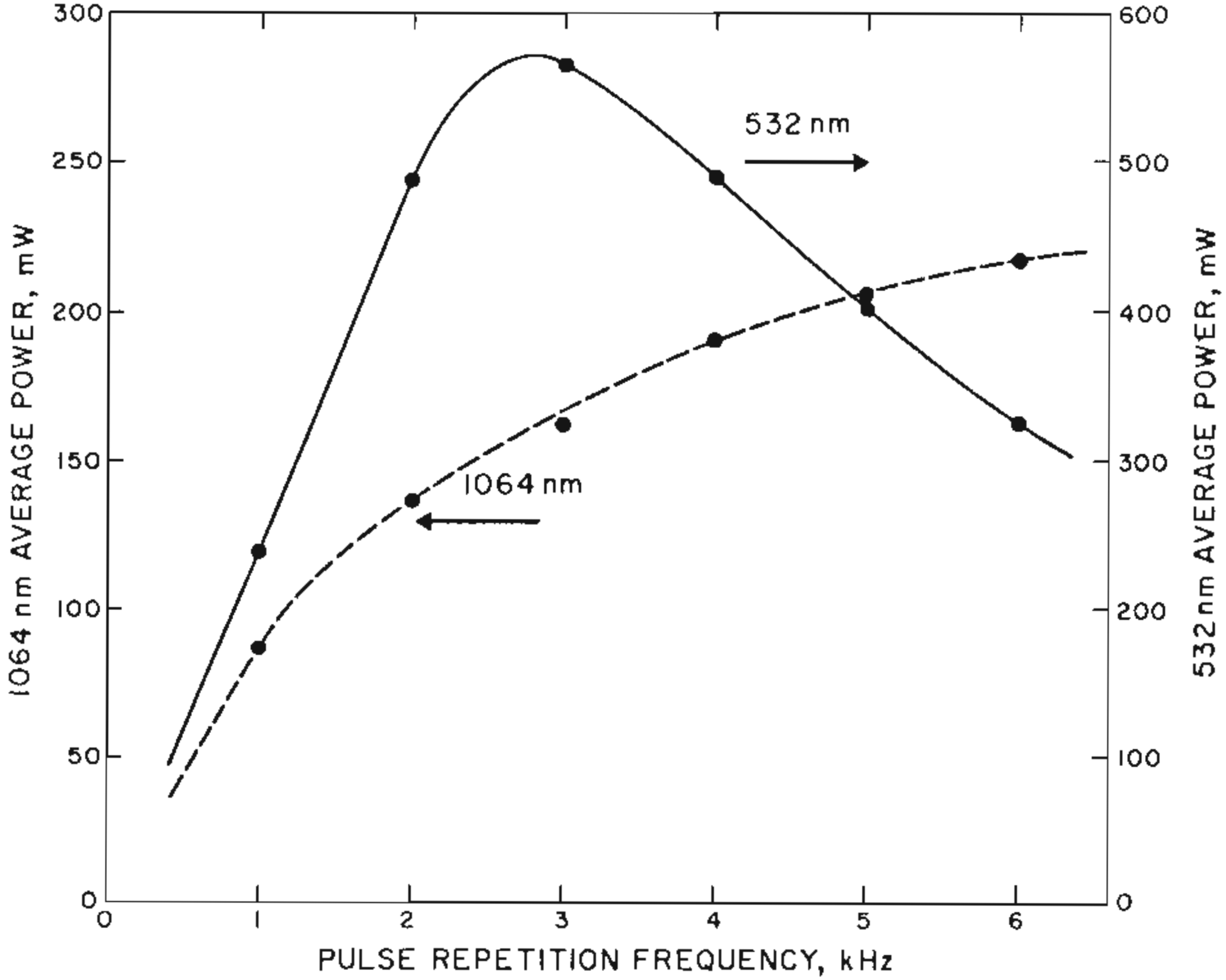

Figure 4-2. Average output powers at 532 nm and 1064 nm as provided by the cw-pumped Nd:YAG laser Q-switched at various repetition frequencies.

90° to the polarization plane of the second harmonic. This component also served as the pump in the mixer. The shapes of the 1064 nm and 532 nm average power curves as a function of pulse rate generally resemble those reported elsewhere[68] with only the second harmonic coupled out of the cavity. For comparison purposes, at the excitation level for which the data of Figure 4-2 were measured, the laser produced a 1064 nm TEM_{00} output of 2.5 W cw with the $LiIO_3$ crystal removed and the acoustooptic Q-switch turned off.

Figure 4-3 shows the corresponding ultraviolet average powers generated by the KD*P and KDP crystals, as measured with a bolometric power meter.[71] The optimum Q-switch frequency was between 2 and 3 kHz, where about 22 mW at 266 nm and 2.1 mW at 213 nm were obtained. As expected, the optimum UV pulse rates were in close agreement with the rate that produced the highest 532 nm average power in Figure 4-2. It should be noted that the optical losses in the experiment were such that 88 percent of the 532 nm power given in Figure 4-2 entered the KD*P doubler, while 64 percent of the 1064 nm power of Figure 4-2 and 78 percent of the 266 nm power of Figure 4-3 entered the KDP mixer. The conversion efficiency for the 532 nm/266 nm process was about 5 percent and the 266 nm/213 nm efficiency was about 12 percent at the lower pulse repetition frequencies.

Measurements of the pulse durations with fast silicon and vacuum photodiodes and a Tektronix 7904 oscilloscope indicated that the infrared pulse length was about 175 nsec at repetition rates below

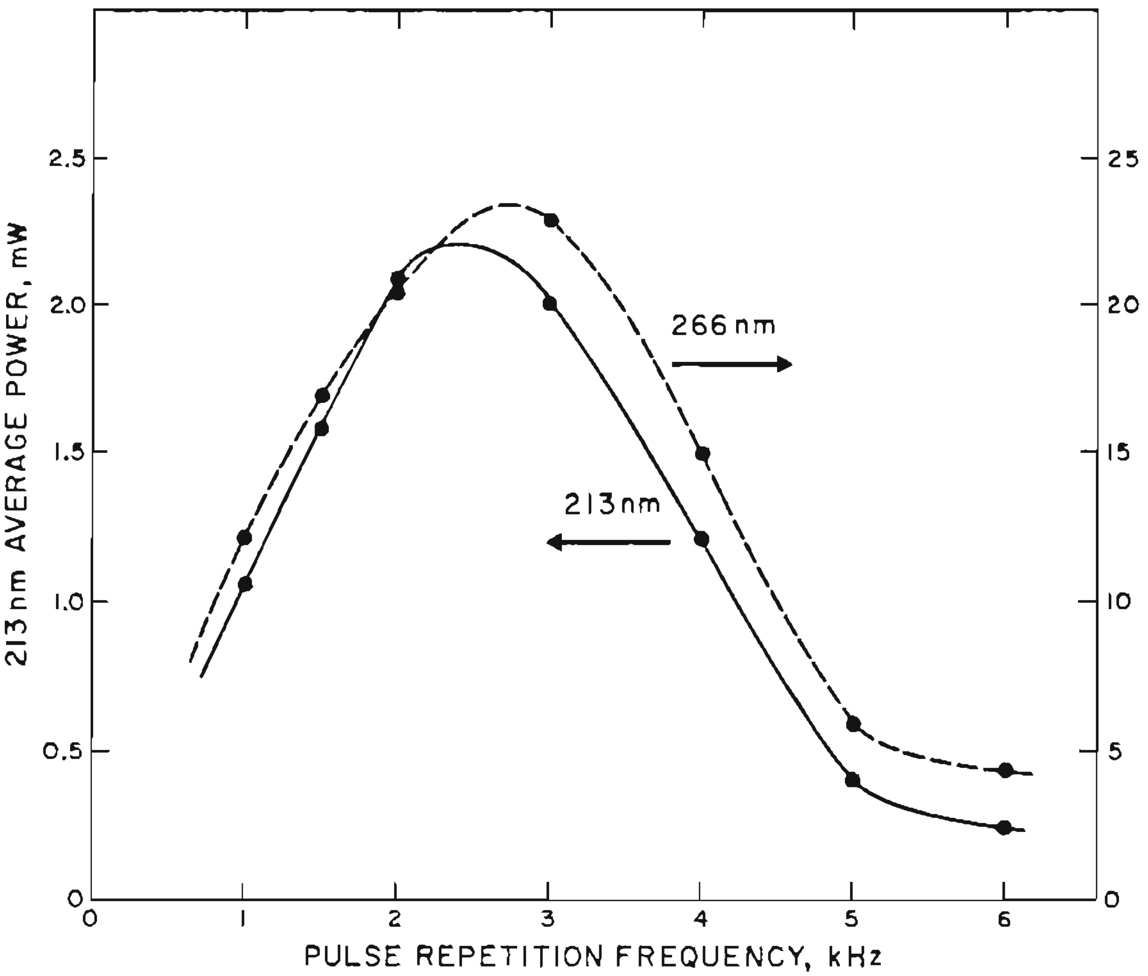

Figure 4-3. Average output powers at 266 nm and 213 nm provided by the cw-pumped Nd:YAG laser Q-switched at various frequencies.

3 kHz, rising to 200 ns at 4 kHz and 290 ns at 6 kHz. The 532 and 266 nm pulses were 0.7 and 0.5 times the length of the 1064 nm pulses, respectively. Typical fifth-harmonic pulse durations were between 60 and 80 ns. The envelopes of the pulses were essentially Gaussian, with considerable intermode beat modulation in most of the UV pulses. Pulse lengths were sensitive to resonator losses; slight adjustment of the mirror alignment could easily change the pulse duration by 10 percent.

The UV average power generated by this nonlinear scheme is greater than the ~ 1 mW required for linear photoemission microscopy. Its best duty factor is about 2×10^{-4} (i.e., 3 kHz × 80 ns) so that the peak current densities produced would be 2×10^{-5} A/cm^2 $\times (2 \times 10^{-4})^{-1} = 0.1$ A/cm^2, below the value for which space charge aberrations become objectionable.

4.3. Photoelectron Microscopy with the Nd:YAG Laser UV Source

The ultraviolet wavelengths produced by the illuminator described above have been used to obtain electron micrographs in a high vacuum photoelectron microscope.[72] The UV beam was focused onto the samples using simple fused silica lenses. Figure 4-4 shows the photoelectron image of a gold-coated replica grating obtained with 213 nm illumination. The average UV power was ~ .1 mW at a pulse rate of 3 kHz and the beam was focused to a spot about 7 μm in diameter at the sample. To obtain uniform illumination across

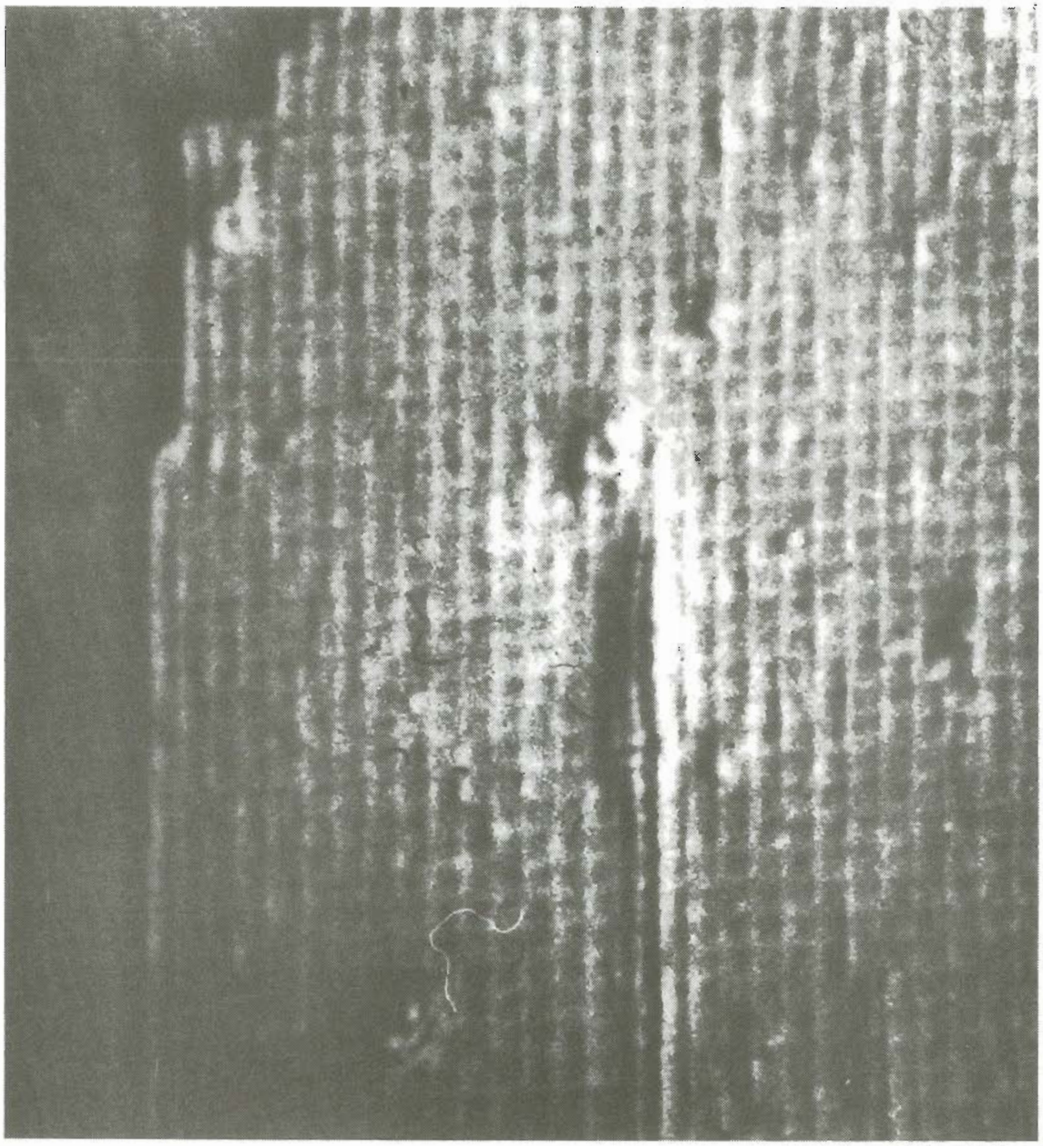

Figure 4-4. Photoelectron micrograph of gold mesh pattern illuminated at 266 nm.

the surface the optical spot was scanned slowly across the surface during the exposure.

The 266 nm radiation has also been used and Figure 4-5 shows the same replica grating as Figure 4-4 using 266 nm illumination. The laser beam was defocused to a diameter greater than the field of view, producing somewhat uneven illumination. The average power was ~ 2 mW at a pulse rate of 4 kHz spread into a 150 μm diameter spot.

These results show that the UV produced by the nonlinear scheme described earlier can be used as a focusing illuminator in nonlinear photoemission experiments. This UV source has the additional advantage that it can provide radiation for use in the nonlinear experiments as well. The electron micrographs demonstrate also that the duty factor associated with this laser is suitable for imaging with resolutions in the range 500-1000 Å.

4.4. Nonlinear Photoelectron Emission Imaging

The nonlinear emission processes described in Chapter 2 have been used to form images of waves propagating in both GaAs and $LiNbO_3$. In this section, these results will be presented. First, the electron optical system used will be described and then the experimental conditions under which the images were obtained will be discussed.

The nonlinear emission was viewed with a simple electron system based on a modified type 6032 electrostatic image tube. The 6032 is

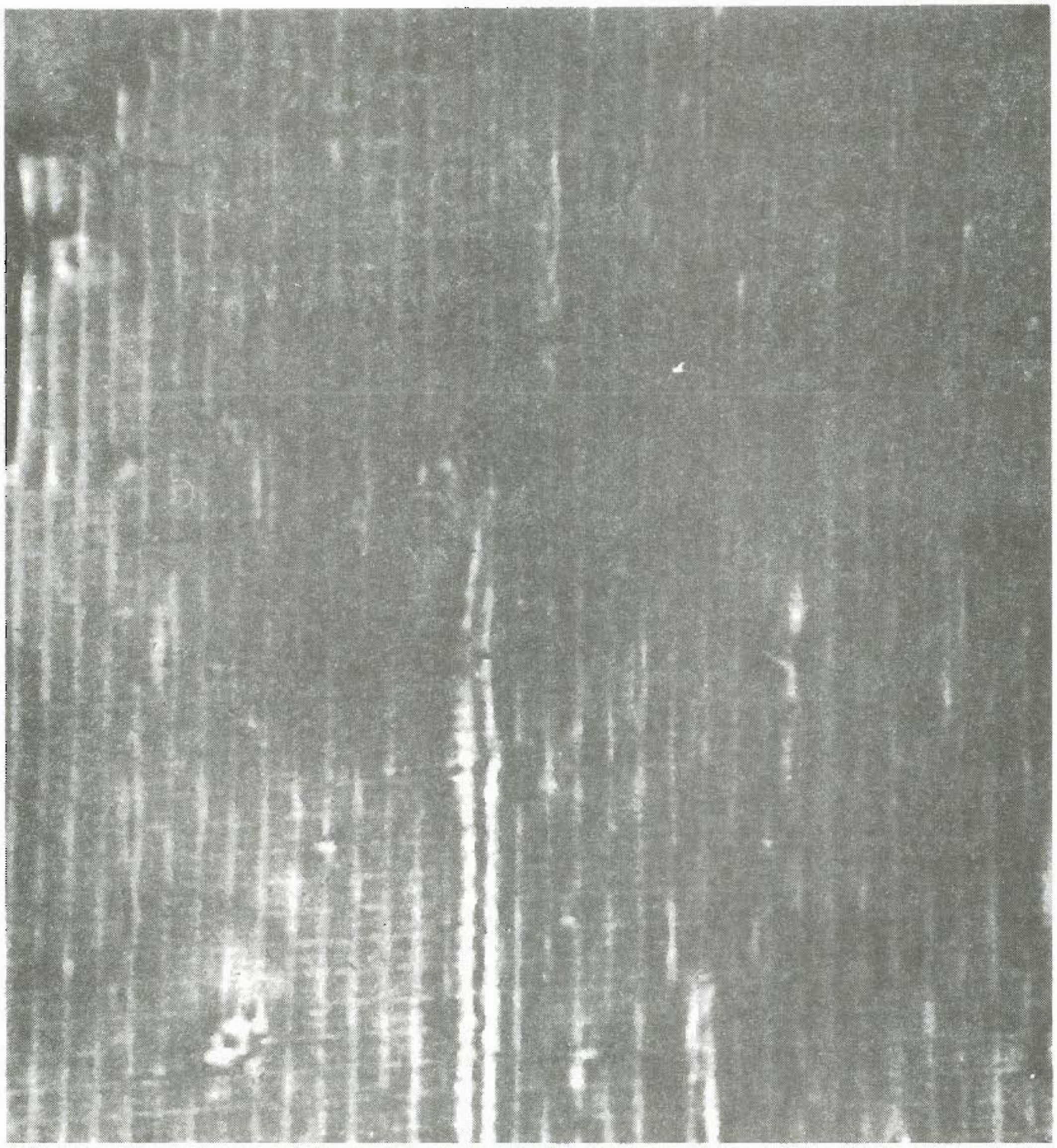

Figure 4-5. Photoelection micrograph of gold mesh pattern illuminated at 213 nm.

a three-electrode tube with electrostatic focusing. The cathode of the image tube was removed and replaced by the sample, and the phosphor screen of the original tube was replaced by a channel plate electron multiplier backed by a new phosphor screen. The electron optics are shown schematically in Figure 4-6. The electron optics provided an overall magnification of 0.5 and a resolution of ~ 1 mm. Images on the screen were observed and photographed through a viewing port in the side of the chamber. The electron optics and the sample were mounted in the bell jar vacuum system mentioned in Chapter 2.

Images of the nonlinear electron emission from $LiNbO_3$ and GaAs have been obtained. The $LiNbO_3$ sample was prepared so that the exciting light beam could enter through a polished edge. The angle of the beam was such that it was guided by total internal reflection between the polished faces of the crystal. Under these conditions the fields outside the crystal are evanescent and no light is radiated from the faces. This arrangement is shown in Figure 4-7. A conducting layer was applied to the emission face of the crystal by the procedure of Section 3.4. A 532 nm beam produced by the continuously pumped laser was focused to a diameter of 0.1 mm at the sample. At intensities corresponding to about 10 $\mu A/cm^2$ photocurrent densities ($I \sim 1$ MW/cm^2), useful images were produced; such an image is shown in Figure 4-8. The multiple spots corresponding to areas of intersection of the guided beam with the $LiNbO_3$ surface

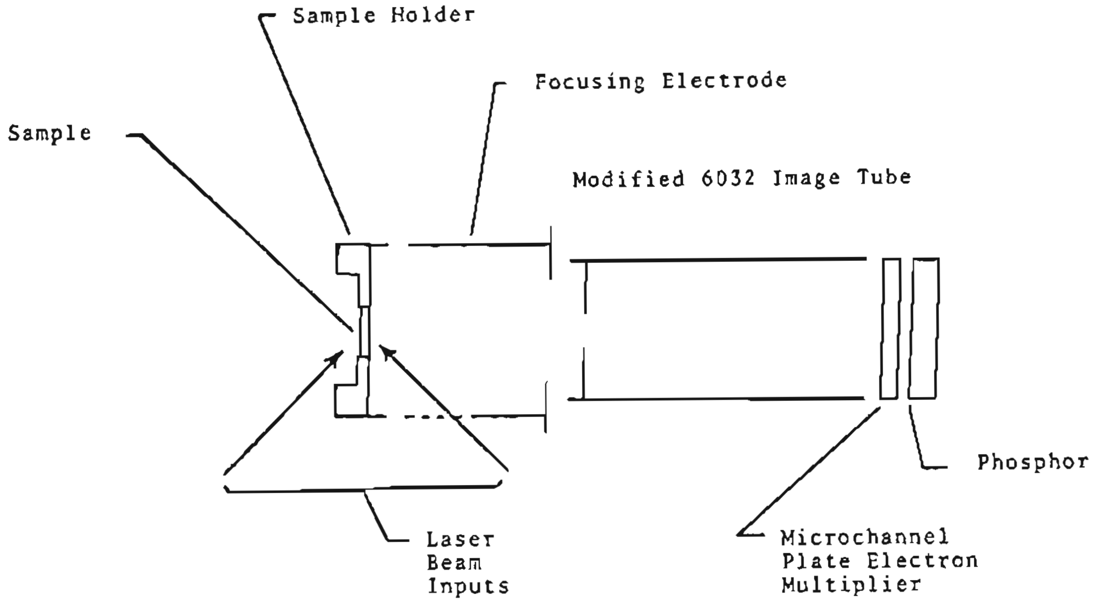

Figure 4-6. Low magnification imaging experiment.

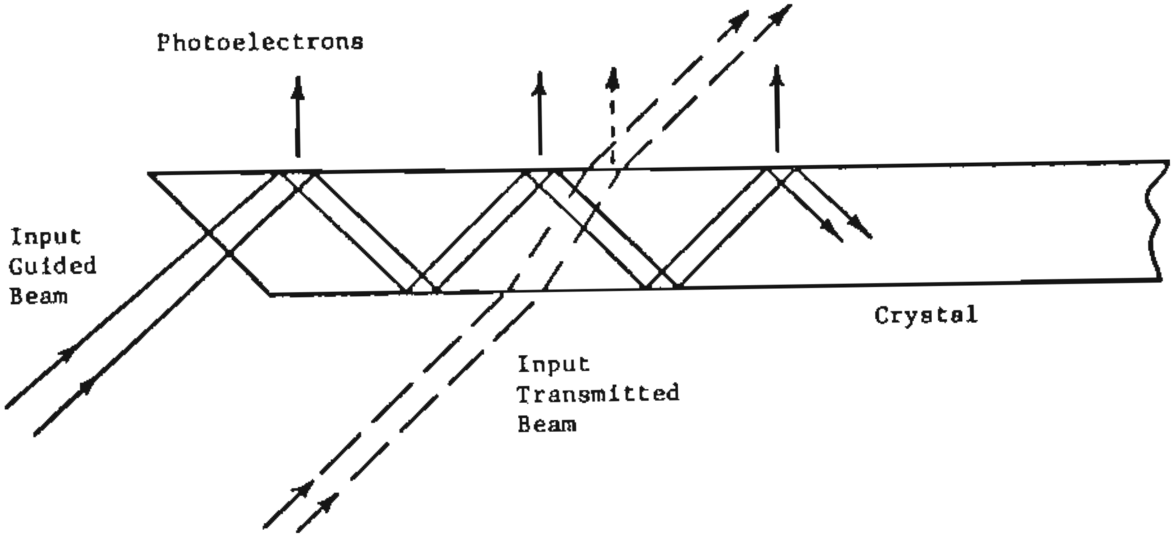

Figure 4-7. Sample geometry for photoelectron imaging experiments.

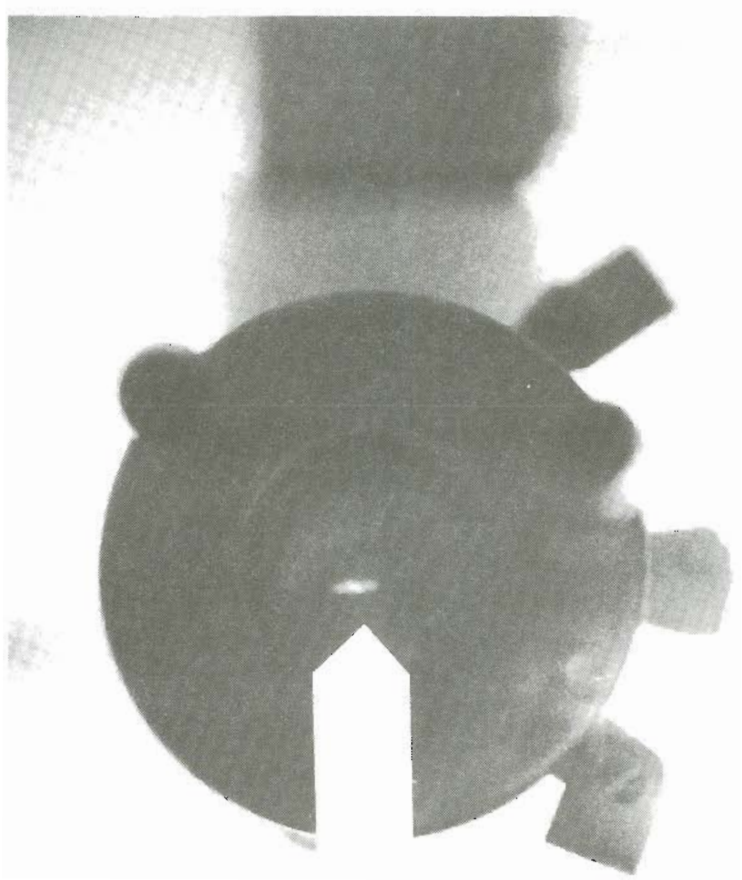

Figure 4-8. Photoemission image of internally guided beam in $LiNbO_3$. Multiple reflections of beam against surface are indicated by arrow.

are clearly visible. Images were also obtained with the laser beam incident on the emission face of the crystal.

Imaging experiments with an uncoated (110) GaAs sample, illuminated at 1064 nm, were also carried out. Photocurrent densities of $\sim 10\ \mu A/cm^2$ were produced by optical intensities of $\sim 10\ MW/cm^2$. An image of a 1064 nm beam incident on the emission face of a GaAs sample is displayed in Figure 4-9.

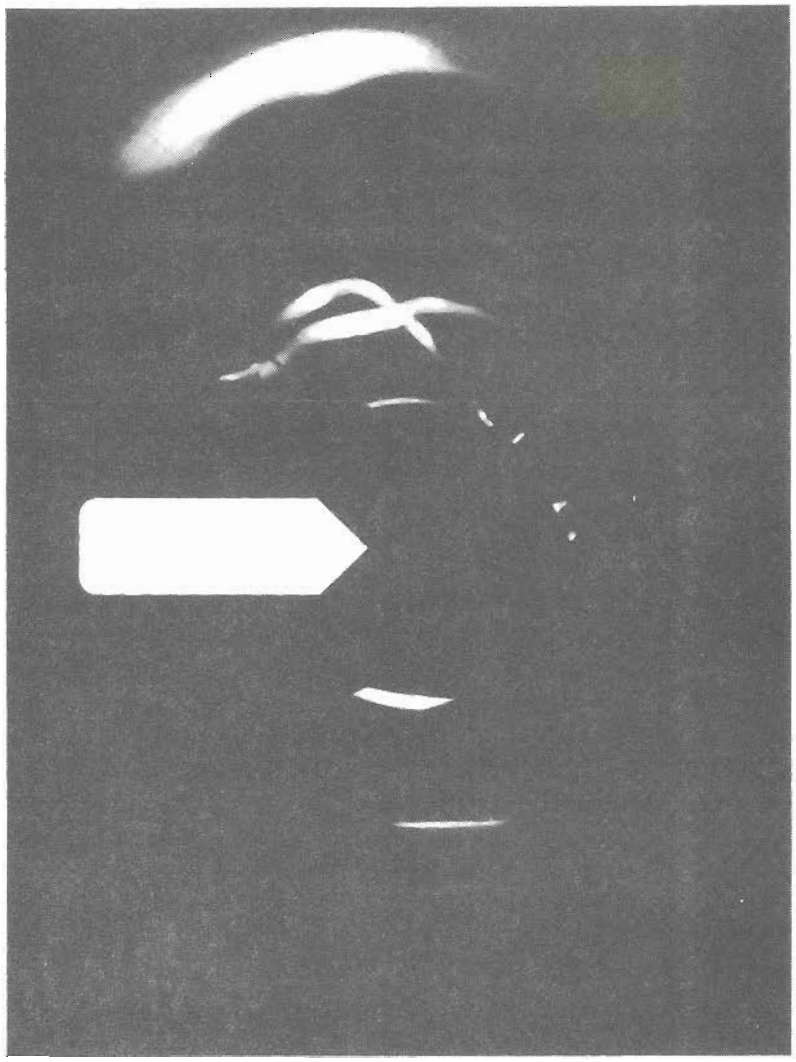

Figure 4-9. Photoemission image of GaAs produced by 1064 nm radiation.

CHAPTER 5

SUMMARY

Nonlinear photoemission mechanisms have been investigated for GaAs and $LiNbO_3$ and their nonlinear photoelectric yield characteristics have been obtained. These yields were achieved using several different sample preparation techniques. GaAs was used as a bare, polished crystal with or without a thin layer of cesium applied to the surface. The $LiNbO_3$ samples investigated were polished crystals coated with a thin tungsten layer alone, or with an additional thin layer of cesium. The coatings used were measured to be highly transparent and to have thicknesses very much less than visible light wavelengths; hence guided waves propagating in $LiNbO_3$ or GaAs substrate were able to penetrate the coating layer. The current densities required for high resolution imaging can be produced by the nonlinear emission in these materials with optical intensities below the damage threshold. Simple, low-resolution electron optics have been used to form images of waves propagating in samples of GaAs and $LiNbO_3$.

An ultraviolet illuminator suitable for linear photoemission microscopy has been developed and used to obtain high resolution electron micrographs at wavelengths of 266 and 213 nm. This ultraviolet source is useful for obtaining an image of the sample to be studied using nonlinear emission and also provides illumination for operator adjustment of the electron optics. The duty factor of this illuminator is virtually the same as that of the laser source used in obtaining the low resolution, nonlinear photoelectron images. We therefore have experimental evidence that the duty factor of the continuously pumped, repetitively Q-switched Nd:YAG laser is adequate for high resolution imaging. This result is independent of the aberration theory developed in Chapter 3.

The aberrations introduced into photoelectron emission imaging by the use of high current density electron beams were considered in detail in Chapter 3. Many different physical processes occurring in the anode-cathode space in the photoelectron microscope have been analyzed and the parametric dependence of the image aberrations has been found. These results indicate that aberrations will introduce image blur of less than ~ 500 Å for current densities as high as 1 A/cm^2 in narrow beams. Nonlinear photocurrent densities much less than 1 A/cm^2 are needed for submicron imaging, and these space charge dependent aberrations should not be limiting factors in obtaining image resolutions down to 500 Å.

REFERENCES

1. E. Brüche, "Elektronenmikroskopische Abbildung mit lichtelektrischen Elektronen," Z. Phys. 86, 448, 1933.
2. O. H. Griffith, G. H. Lesch, G. F. Rempfer, G. B. Birrell, C. A. Burke, D. W. Schlosser, M. H. Mallon, G. B. Lee, R. G. Stafford, P. C. Jost, and T. B. Marriott, "Photoelectron Microscopy: A New Approach to Mapping Organic and Biological Surfaces," Proc. Nat. Acad. Sci. USA 69, 561-575, 1972.
3. W. Engel, "Emission Microscopy with Different Kinds of Electron Emission," Proc. Sixth International Congress for Electron Microscopy, Kyoto, Japan, p. 217-218, 1966.
4. P. V. Fontana, J. P. Decosterd, and L. Wegmenn, "Investigations of Carbon Residues on Surfaces of Silicon Integrated Circuits," J. Electrochem. Soc. 121, 146-150, 1974.
5. W. Engel and S. Grund, "Photoelectron Emission Microscopy of Biological Specimens," Proc. Eighth International Congress on Electron Microscopy, Canberra, Australia, p. 656-657, 1974.
6. M. D. Crisp, "Laser Induced Surface Damage of Transparent Dielectrics," IEEE J. Quantum Electron. QE-10, 57-62, 1974.
7. N. Bloembergen, "Role of Cracks, Pores, and Absorbing Inclusions on Laser Induced Damage Threshold at Surfaces of Transparent Dielectrics," Appl. Opt. 12, 661-664, 1973.
8. H. Sonnenberg, H. Heffner, and W. Spicer, "Two-Photon Photoelectric Effect in Cs_3Sb," Appl. Phys. Lett. 5, 95-96, 1964.

9. S. Imamura, F. Shiga, K. Kinoshita, and T. Suzuki, "Double-Photon Photoelectric Emission from Alkali Antimonides," Phys. Rev. 166, 322-323, 1968.

10. E. M. Logothetis, "Two-Photon Photoelectric Spectroscopy in CsI," Phys. Rev. Lett. 19, 1470-1472, 1967.

11. E. M. Logothetis and P. L. Hartman, "Three Photon Photoelectric Effect in Gold," Phys. Rev. Lett. 18, 581-583, 1967.

12. Gy. Farkas, I. Kertész, W. Náray, and P. Varga, "On the Laser-Induced Non-Linear Photoelectric Effect in Metals," Phys. Lett. 25A, 572-573, 1967.

13. J. H. Bechtel, W. L. Smith, and N. Bloembergen, "Two-Photon Photoemission from Metals Induced by Picosecond Laser Pulses," Phys. Rev. B 15, 4557-4563, 1977.

14. M. C. Teich, J. M. Schroeer, and G. J. Wolga, "Double-Quantum Photoelectric Emission from Sodium Metal," Phys. Rev. Lett. 13, 611-614, 1964.

15. A. H. Sommer, Photoemissive Materials, John Wiley and Sons, New York, 1968, Chapter 2.

16. A. van der Ziel, Solid State Physical Electronics, 3rd. Ed., Prentice Hall, Englewood Cliffs, N.J., Chapter 7.

17. E. O. Kane, "Implications of Crystal Momentum Conservation in Photoelectric Emission for Band Structure Measurements," Phys. Rev. Lett. 12, 97-98, 1964.

18. C. N. Berglund and W. E. Spicer, "Photoemission Studies of Copper and Silver: Theory," Phys. Rev. 136. A1030-1044, 1964.

19. G. D. Mahan, "Theory of Photoemission in Simple Metals," Phys. Rev. B 2, 4334-4350, 1970.

20. M. L. Cohen and T. K. Bergstrasser, "Band Structures and Pseudopotential Form Factors for Fourteen Semiconductors of the Diamond, and Zinc-blende Structures," Phys. Rev. 141, 789-796, 1966.

21. W. E. Spicer and R. C. Eden, "Photoemission Investigation of the Band Structure of Semiconductors," Proc. IX International Conference on the Physics of Semiconductors," Moscow, USSR, 1, 65-91, 1968.

22. K. Bärner, R. Braunstein, and H. H. Weakliem, "The Optical Properties of $LiNbO_3$," Phys. Status Solidi B 68, 525-530, 1975.

23. G. W. Gobeli and F. G. Allen, "Photoelectric Properties of Cleaned GaAs, GaSb, InAs, and InSb Surfaces: Comparison with Si and Ge," Phys. Rev. 137, A245-A254, 1965.

24. A. A. Akhazen, A. N. Brozdnichenko, and E. V. Bursian, "Influence of the Spontaneous Polarization on the Photoelectric Emission from Lithium Niobate," Sov. Phys.-Solid State 20, 912, 1978.

25. J. J. Hopfield, J. M. Warlock, and K. Park, "Two-Quantum Absorption Spectrum of KI," Phys. Rev. Lett. 11, 414-417, 1963.

26. E. M. Logothetis, "Two-Photon Photoelectric Spectroscopy in CsI," Phys. Rev. Lett. 19, 1470-1472, 1967.

27. R. H. Pantell and H. E. Puthoff, Fundamentals of Quantum Electronics, John Wiley and Sons, New York, 1969, Chapter 5.

28. Ibid.

29. N. M. Bityurin, V. I. Bredikhin, and V. N. Genkin, "Nonlinear Optical Absorption and Energy Structure of $LiNbO_3$ and α-$LiIO_3$ Crystals," Sov. J. Quantum Electron. 8, 1377-1379, 1978.

30. J. H. Bechtel, "Heating of Solid Targets with Laser Pulses," J. Appl. Phys. 46, 1585-1593, 1975.

31. G. A. Massey and J. C. Johnson, "Gain Limitations in Optical Parametric Amplifiers," IEEE J. Quantum Electron. QE-15, 201-203, 1979.

32. E. Brüche, "Elektronenmikroskopische Abbildung mit lichtelektrischen Elektronen," Z. Phys. 86, 448, 1933.

33. M. Knoll and E. Ruska, "Das Elektronenmikroscop," Z. Phys. 78, 318-339, 1932.

34. W. Engel, "Emission Microscopy with Different Kinds of Electron Emission," Proc. Sixth International Contress for Electron Microscopy, Kyoto, Japan, p. 217-218, 1966.

35. W. Engel and S. Grund, "Photoelectron Emission Microscopy of Biological Specimens," Proc. Eighth International Congress on Electron Microscopy, Canberra, Australia, p. 656-657, 1974.

36. G. A. Massey, B. P. Plummer, and J. C. Johnson, "A High Repetition Rate for Laser Spanning the 195-225 nm Spectral Region," IEEE J. Quantum Electron. QE-14, 673-679, 1978.

37. M. D. Jones and G. A. Massey, "Milliwatt-Level 213 nm Source Based on a CW-Pumped Nd:YAG Laser," IEEE J. Quantum Electron. QE-15, 204-206, 1978.

38. K. Jain, "A Milliwatt-Level CW Laser Source at 224 nm," Appl. Phys. Lett. 36, 10-11, 1980.

39. A. van der Ziel, Solid State Physical Electronics, 3rd Ed., Prentice Hall, Englewood Cliffs, N.J., p. 172.

40. V. N. E. Robinson, "The Elimination of Charging Artifacts on the Scanning Electron Microscope," J. Phys. E 8, 62-64, 1975.

41. G. E. Pfefferkorn, H. Gruter, and M. Pfautsch, "Observations on the Prevention of Specimen Charging," Proc. SEM Symposium, p. 147-152, 1972.

42. L. Weber and H. R. Oswald, "Physical Factors Affecting the Investigation of Non-Metals by Means of Photo-Emission Electron Microscopy," Optik 45, 333-343, 1976.

43. P. Lorrain and D. R. Corson, Electromagnetic Fields and Waves, W. H. Freeman and Co., San Francisco, 1970, p. 424.

44. G. A. Massey, N. G. Eror, and G. W. Nelson, "Measurement of Very High Resistivities Using Electrooptic Crystals," Appl. Opt. 19, 1282-1284, 1980.

45. A. van der Ziel, Solid State Physical Electronics, 3rd Ed., Prentice Hall, Englewood Cliffs, N.J., p. 226.

46. A. H. Sommer, Photoemissive Materials, John Wiley and Sons, New York, 1968, p. 57.

47. O. Klemperer and M. E. Barnett, Electron Optics, 3rd Ed., Cambridge University Press, London, 1971, Chapters 6 and 7.

48. P. Grivet, Electron Optics, Part 1, Optics, 2nd English Ed., Pergamon Press, Oxford, 1972, Chapter 7.

49. B. P. Plummer, "Ultraviolet Laser Sources for Photoelectron Microscopy," Ph.D. Dissertation, Oregon Graduate Center, 1979.

50. Ibid., p. 53.

51. H. Boersch, "Experimentalle Bestimmung der Energieverteilung in thermisch ausgelösten Elektronenstrahlung," Z. Phys. 139, 115-146, 1954.

52. B. Zimmermann, Advances in Electronics and Electron Physics 29, L. Marton, Ed., Academic Press, New York, 1970, p. 257-312.

53. A. V. Crewe, "Some Space Charge Effects in Electron Probe Devices," Optik 52, 337-346, 1979.

54. T. Groves, D. L. Hammond, and H. Kuo, "Electron Beam Broadening Effects Caused by Discreteness of Space Charge," J. Vac. Sci. Technol. 16, 1680-1685, 1979.

55. W. Knauer, "Analysis of Energy Broadening in Electron and Ion Beams," Optik 54, 211-234, 1979.

56. E. DeChambost and C. Hennion, "Energy Broadening in and Electron Gun. Theoretical Model and Experimental Results," Optik 55, 357-370, 1980.

57. K. H. Loeffler, "Energy-Spread Generation in Electron-Optical Instruments," Z. Angew. Phys. 27, 145-149, 1969.

58. A. Papoulis, Probability, Random Variables, and Stochastic Processes, McGraw Hill, New York, 1965, p. 287.

59. H. Goldstein, Classical Mechanics, Addison-Wesley, Reading, Mass., 1950, p. 62.

60. R. J. Dam and O. H. Griffith, "Photoelectron Microscopy of Biological Surfaces: Excitation Source Brightness Requirements," Proc. Soc. Photo-Opt. Instrum. Eng., 78, 143-154, 1976.

61. B. P. Plummer, "Ultraviolet Laser Sources for Photoelectron Microscopy," Ph.D. Dissertation, Oregon Graduate Center, 1979, Chapter 4.

62. A. H. Sommer, Photoemissive Materials, John Wiley and Sons, New York, 1968. p. 21-26.

63. G. A. Massey, B. P. Plummer, and J. C. Johnson, "A High Repetition Rate Ion Laser Spanning the 195-225 nm Spectral Region," IEEE J. Quantum Electron. QE-14, 673-679, 1978.

64. J. B. Marling, "Ultraviolet Ion Laser Performance and Spectroscopy, Part I: New Strong Noble-Gas Transitions Below 2500 Å," IEEE J. Quantum Electron. QE-11, 822-834, 1975.

65. J. R. McNeil, W. L. Johnson, and G. J. Collins, "Ultraviolet Laser Action in He-Ag and Ne-Ag Mixtures," Appl. Phys. Lett. 29 172-174, 1976.

66. G. A. Massey, M. D. Jones, and J. C. Johnson, "Generation of Pulse Bursts at 212.8 nm by Intracavity Modulation of an Nd:YAG Laser," IEEE J. Quantum Electron. QE-14, 527-532, 1978.

67. J. H. Bechtel, "Heating of Solid Targets with Laser Pulses," J. Appl. Phys. 46, 1585-1593, 1975.

68. R. B. Chesler, M. A. Karr, and J. E. Geusic, "Repetitively Q-Switched Nd:YAG-$LiIO_3$ 0.53-μ Harmonic Source," J. Appl. Phys. 41, 4125-4127, 1970.

69, G. H. Lesch, J. C. Johnson, and G. A. Massey, "A Thermostatic Control System for Nonlinear Optical Experiments at Low Temperatures, IEEE J. Quantum Electron. QE-12, 83-86, 1976.

70. F. Zernike and J. E. Midwinter, Applied Nonlinear Optics, John Wiley and Sons, New York, 1973, p. 61.

71. J. C. Johnson and G. A. Massey, "Bolometric Laser Power Meter for Sensitive Measurements in the IR-UV Spectral Range," Appl. Opt. 17, 2268-2269, 1978.

72. O. H. Griffith, H. M. Brown, and G. H. Losch, "Photoelectron Microscopy of Photosynthetic Membranes," in Light Transducing Membranes: Structure, Function and Evolution, D. Dearner, Ed., Academic Press, Inc., New York, p. 313-334, 1978.

APPENDIX A

COMPUTER PROGRAM FOR DETERMINING TIME OF FLIGHT CHANGE PRODUCED BY THE DETERMINISTIC SPACE CHARGE FIELD

```
C     *************************************

C     TIME OF FLIGHT ABERRATION:DETERMINISTIC FIELD
C
C
C
C
C     ONE DIMENSIONAL MOTION OF ELECTRON THROUGH AN ARBITRARY
C     PERTURBING FIELD IN A UNIFORM FIELD
C
C
C     ZK=2*E/M
C     Z=FIELD POSITION IN MICRONS
C     EZ=FIELD PERTURBATION IN V/CM
C     ZDOT=ELECTRON SPEEED IN MICRONS/PSEC
C     E0=UNIFORM FIELD IN V/CM
C     T=TOTAL TIME OF FLIGHT IN PSEC
C
C     THE UNIFORM FIELD IS ANODE VOLTAGE/DISTANCE
C
C     THE SPEED AT EACH POINT Z(I) IS EVALUATED FROM
C       ZDOT(I)=SQRT((2E/M)EZ(I)(Z(I+1)-Z(I))+ZDOT(I)**2)
C
C
C     THE TIME OF FLIGHT IS
C       2*SUM((Z(I+1)-Z(I))/(ZDOT(I)+ZDOT(I+1))
C
C
C     **************************************


      DOUBLE PRECISION Z(20),EZ(20),ZDOT(20),ZK,E0,T

C     FIELD DATA ARE FROM PLUMMER THESIS.
      DATA Z/0.,.1,1.,2.,3.,4.,5.,10.,15.,20.,25.,30.,40.,50.,
     1 100.,300.,500.,1000.,2000.,4000./

      DATA EZ/-25.49,-22.23,-16.38,-10.53,-6.94,-5.06,-3.18,-.47,
     1 -.08,.22,.25,.26,.23,.20,.10,.03,.02,.01,.0,.0/



      ZK=3.51769D-5
      E0=75000.

      CALL CONTRL(2,'FLIGHT',11,0)
```

```
      WRITE(11,8)


      DO 300 KK=1,9
C     CALCULATE THE SPEED ST EACH Z(I).


      ZDOT(1)=0.0
       DO 100 I=1,19
        AJ=(10.**(KK-5))*1.27
        ZDOT(I+1)=DSQRT(((Z(I+1)-Z(I))*ZK*(EZ(I)*10.**(KK-5)+E0)
     1  +ZDOT(I)**2))
  100  CONTINUE

C     CALCULATE THE TIME OF FLIGHT

       T=0.0
       DO 200 K=1,19
        I=20-K
        T=T+2.*(Z(I+1)-Z(I))/(ZDOT(I+1)+ZDOT(I))
  200  CONTINUE

C     OUTPUT THE TIME OF FLIGHT.

       WRITE(11,10) AJ,T
  300 CONTINUE
   10 FORMAT(F20.3,5X,F20.6)
    8 FORMAT(10X,' CURRENT DENSITY ',9X,'TIME OF FLIGHT',/
     1 10X,' AMP/CM2 ',16X,' PSEC ')
      CALL CONTRL(4,0,11,0)

      CALL EXIT
      END
```

APPENDIX B

COMPUTER PROGRAM FOR DETERMINING TIME OF FLIGHT CHANGE PRODUCED BY THE STATISTICAL SPACE CHARGE FIELD

```
C     *********************************
C     TIME OF FLIGHT ABERRATION:STATISTICAL FIELD
C
C
C
C
C     ONE DIMENSIONAL MOTION OF ELECTRON THROUGH AN ARBITRARY
C     PERTURBING FIELD IN A UNIFORM FIELD
C
C
C     Z=FIELD POSITION IN MICRONS
C     EZ=FIELD PERTURBATION IN V/CM
C     ZDOT=ELECTRON SPEEED IN MICRONS/PSEC
C     EO=UNIFORM FIELD IN V/CM
C     T=TOTAL TIME OF FLIGHT IN PSEC
C
C     THE UNIFORM FIELD IS ANODE VOLTAGE/DISTANCE
C
C     THE SPEED AT EACH POINT Z(I) IS EVALUATED FROM
C       ZDOT(I)=SQRT((2E/M)EZ(I)(Z(I+1)-Z(I))+ZDOT(I)**2)
C
C
C     THE TIME OF FLIGHT IS
C       2*SUM((Z(I+1)-Z(I))/(ZDOT(I)+ZDOT(I+1))
C
C
C
C
C     PROGRAM EVALUATES TIME OF FLIGHT CHANGE PRODUCED
C     BY STATISTICAL E FIELD (Z COMPONENT)
C
C     THE FIELD IS GIVEN BY EZ(Z)=15.864/Z**.416
C     CALCULATIONS BASD ON J=1 AMP/CM**2
C
C**************************************


      DOUBLE PRECISION Z ,ZDOT1,ZDOT2,EO,EZ,T,ZK
      ZK=3.51769D-5
      EO=75000.
      Z=0.0
      ZDOT1=0.0

      EZ=0.0
      T=0.0
```

```
      DO 100 I=1,20000
       Z=.2*I
       EZ=15.864/(Z**.417)
       ZDOT2=DSQRT((.2*ZK*(EZ+E0)+ZDOT1**2))
       T=T+.4/(ZDOT1+ZDOT2)
       ZDOT1=ZDOT2


  100 CONTINUE


      CALL CONTRL(2,'FLIGHT',11,0)
      WRITE(11,10) T
   10 FORMAT('THE TIME OF FLIGHT IN PSEC IS ',E21.7)
      CALL CONTRL(4,0,11,0)
      CALL EXIT
      END
```

VITA

Michael D. Jones was born in Bartlesville, Oklahoma on March 25, 1950. He received the A.B. and A.M. degrees from Washington University, St. Louis, in 1972 and 1974 respectively and studied at the University of Oregon during 1972-1973.

Mr. Jones taught physics, chemistry and general science at Mary Institute, St. Louis, from 1974 to 1977. During this period he was also an instructor at Forest Park Community College. In 1977 he began his studies at the Oregon Graduate Center and was awarded a Wilson Clark Fellowship in 1978.